PHYSICAL REVIEW B **106**, 115134 (2022)

Random strain induced correlations in materials with intertwined nematic and magnetic orders

W. Joe Meese,[1] Thomas Vojta,[2] and Rafael M. Fernandes[1]
[1]*School of Physics and Astronomy, University of Minnesota, Minneapolis, Minnesota 55455, USA*
[2]*Department of Physics, Missouri University of Science and Technology, Rolla, Missouri 65409, USA*

(Received 21 December 2021; revised 8 July 2022; accepted 7 September 2022; published 19 September 2022)

Electronic nematicity is rarely observed as an isolated instability of a correlated electron system. Instead, in iron pnictides and in certain cuprates and heavy-fermion materials, nematicity is intertwined with an underlying spin-stripe or charge-stripe state. As a result, random strain, ubiquitous in any real crystal, creates both random-field disorder for the nematic degrees of freedom and random-bond disorder for the spin or charge ones. Here, we put forward an Ashkin-Teller model with random Baxter fields to capture the dual role of random strain in nematic systems for which nematicity is a composite order arising from a stripe state. Using Monte Carlo to simulate this *random Baxter-field model*, we find not only the expected breakup of the system into nematic domains, but also the emergence of nontrivial disorder-promoted magnetic correlations. Such correlations enhance and tie up the fluctuations associated with the two degenerate magnetic stripe states from which nematicity arises, leaving characteristic signatures in the spatial profile of the magnetic domains, in the configurational space of the spin variables, and in the magnetic noise spectrum. We discuss possible experimental manifestations of these effects in iron-pnictide superconductors. Our work establishes the random Baxter-field model as a more complete alternative to the random-field Ising model to describe complex electronic nematic phenomena in the presence of disorder.

DOI: 10.1103/PhysRevB.106.115134

I. INTRODUCTION

Even weak lattice disorder and structural inhomogeneity can substantially alter the properties of electronic ordered states [1,2]. For instance, pair breaking promoted by local impurity scattering strongly reduces the transition temperature of unconventional superconductors [3–5], and impurity-induced phase slips can destroy the long-range order in vortex lattices or incommensurate charge-density waves [6–8]. Because of the unavoidable coupling of the nematic order parameter to lattice deformations, electronic nematicity is particularly sensitive to the intrinsic inhomogeneities of the crystal lattice. Electronic nematic order is characterized by the spontaneous breaking of the rotational symmetry of the system due to electron-electron interactions while the translational symmetry is preserved [9,10]. For tetragonal systems such as cuprates, heavy-fermion materials, and iron-based superconductors, the experimentally observed nematic order has an Ising symmetry, associated with choosing one of the two axes (or one of the two diagonals) of the square basal plane of the unit cell [11]. Due to the electron-phonon coupling, the electronic symmetry breaking is accompanied by a lowering of the tetragonal symmetry of the lattice which undergoes an orthorhombic distortion [12–16]. Such a linear coupling between shear strain and the electronic nematic order parameter renders random strain, which originates from local lattice defects and impurities, a random (Ising) field for the nematic order parameter [11]. As a result, the random-field Ising model (RFIM) has been employed to model nematic-related phenomena in crystals [17–20]. A hallmark of this widely studied model is the complete breakup of the Ising ordered ground state into domains, which takes place for any random-field strength in two-dimensional (2D) systems and beyond a critical disorder strength in three-dimensional (3D) systems [21–24]. More specifically, the RFIM has been invoked to explain puzzling experimental observations in the local density of states of underdoped cuprates [25], in the spin-lattice relaxation rate of iron selenide [26], and in the elastoresistance of doped iron pnictides [27].

Despite the progress in understanding the interplay between nematicity and random strain, one important ingredient has been missing. In many of the tetragonal systems where it has been observed, nematicity is often intertwined with a density-wave type of order that breaks both rotational and translational symmetries [28,29]. In the cuprates $YBa_2Cu_3O_{6+x}$ [30] and $La_{2-x}Sr_xCuO_4$ [31], and in $BaNi_2As_2$ [32] (a relative of the iron-based superconductors), it is a charge-density wave, whereas in the heavy-fermion $CeAuSb_2$ [33] and in the iron-arsenides family [34] ($BaFe_2As_2$, LaFeAsO, and NaFeAs), it is a spin-density wave. In all cases, the density wave tends to be stripelike, characterized by two degenerate ordering vectors $\boldsymbol{Q}_1$ and $\boldsymbol{Q}_2$ related by a fourfold rotation. In analogy with classical liquid crystals, electronic nematicity in these compounds has been proposed to be a vestigial order [29,35] (i.e., a partially melted version) of the underlying density wave, which plays the role of an electronic smectic phase [13,35–44]. As a result, the nematic order parameter is described as a composite density-wave order parameter.

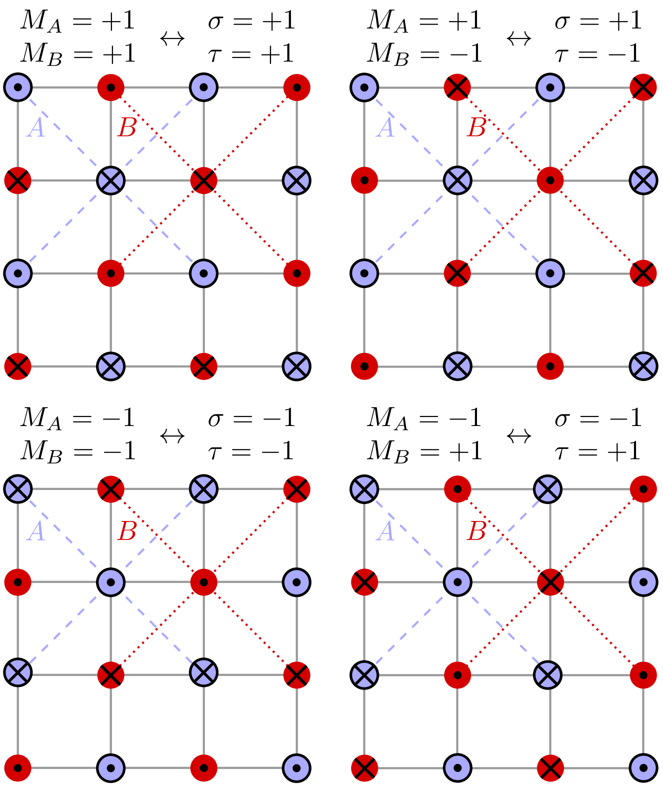

FIG. 1. The fourfold-degenerate stripe-magnetic ground state of the Ising J_1-J_2 model on a square lattice. Blue and red sites denote the A and B sublattices. The magnetic moments point out of the plane. The horizontal (vertical) stripe configuration, corresponding to the ordering vector $\boldsymbol{Q}_H = (0, \pi)$ [$\boldsymbol{Q}_V = (\pi, 0)$], corresponds to parallel (antiparallel) staggered sublattice magnetizations M_A and M_B. These states exhibit either a positive or negative nematic order parameter, defined as the product $\phi \propto M_A M_B$. The staggered magnetizations on the A and B sublattices of the Ising J_1-J_2 model are in one-to-one correspondence with the σ and τ Ising variables of the Ashkin-Teller model. Similarly, the nematic order parameter in the former maps onto the Baxter variable $\sigma\tau$ of the latter.

The composite nature of the nematic order parameter points to a more complex role of random strain that goes beyond the breakup of long-range order into nematic domains. To see this, consider the iron arsenides, for which there is strong evidence that nematic order is a vestige of the stripe-magnetic ground state [45]. The latter has wave vectors $\boldsymbol{Q}_1 = (\pi, 0)$ and $\boldsymbol{Q}_2 = (0, \pi)$ and is described by the staggered magnetizations $\boldsymbol{M}_A$ and $\boldsymbol{M}_B$ of the two sublattices of the square lattice, which can be either parallel or antiparallel to each other (see Fig. 1). The Ising-nematic order parameter ϕ in this case is the composite $\phi = \boldsymbol{M}_A \cdot \boldsymbol{M}_B$ [46]. Random shear strain ϵ therefore plays a dual role. On the one hand, it leads to randomness of the magnetic interactions and thus to random-bond disorder for $\boldsymbol{M}_i$. On the other hand, it couples linearly to ϕ and therefore creates random-field disorder for the nematic order parameter. Because random-field and random-bond effects are quite different, and because there is mutual feedback between the coupled nematic and magnetic degrees of freedom, a description in terms of the RFIM is incomplete.

In this paper, we propose and solve an effective model that, like the RFIM, requires no prior knowledge about microscopic details of the system but, unlike the RFIM, accounts for the dual random-field and random-bond role of random strain in nematic systems for which nematicity is a composite order, rather than an isolated instability. It consists of the Ashkin-Teller Hamiltonian in the presence of a random Baxter field, and is thus dubbed the *random Baxter-field model* (RBFM):

$$H = -\sum_{\langle ij\rangle} [J(\sigma_i\sigma_j + \tau_i\tau_j) + K\sigma_i\tau_i\sigma_j\tau_j] - \sum_i \varepsilon_i\sigma_i\tau_i. \quad (1)$$

Although the model is based on the mapping of the Ising J_1-J_2 model onto the Ashkin-Teller model [47,48], it should be relevant not only for the case where the primary instability is a magnetic stripe state with easy-axis anisotropy, but also when the primary phase is a commensurate charge-stripe phase. Here, the σ and τ Ising variables describe the fourfold-degenerate ground state, consisting of spin-up and spin-down stripes (or, equivalently, charge-rich and charge-poor stripes) aligned along the x and y axes (see Fig. 1). The composite nematic order paramer is given by $\phi = \sigma\tau$, and couples linearly with the shear strain ε. The two energy scales J and K can be directly connected to the J_1 and J_2 exchange constants of the original J_1-J_2 model. We note that this approach is different from and complementary to previous ones where random-field disorder was included only on the primary charge-stripe order [35].

We use a combination of Metropolis and replica-exchange Wang-Landau (WL) Monte Carlo methods to simulate the RBFM on a square lattice. Since both cuprates and iron pnictides are layered systems with relatively large charge-order and magnetic anisotropies, such an approximation is reasonable. Our results not only show a breakup of the system into nematic domains, as in the RFIM, but they also reveal unusual magnetic correlations. Importantly, such correlations are completely absent in the clean case, and arise entirely from the last term in (1), i.e., from the random strain. The key point is that while ε_i completely determines the value of the local nematic order parameter $\sigma_i\tau_i$ (either $+1$ or -1), it allows two different sets $\{\sigma_i, \tau_i\}$ of magnetic order parameters (either $\{+1, +1\}$ and $\{-1, -1\}$ or $\{+1, -1\}$ and $\{-1, +1\}$). Consequently, a particular random strain realization allows multiple $\{\sigma_i, \tau_i\}$ magnetic configurations; in contrast, the RFIM has a single ground state for a given random-field realization.

The consequences of the random strain driven magnetic correlations are multifold. In real space, they cause the system to also break up into magnetic domains. However, the typical sizes of the magnetic domains are larger than those of the nematic domains by a factor of order 2. The disorder-induced magnetic correlations also leave pronounced signatures in the joint $\{\sigma, \tau\}$ distribution in configurational space. In the clean case, as the temperature is lowered, the shape of the typical $\{\sigma, \tau\}$ distribution changes from a circle centered at the origin to four sharp peaks at the vertices of a square. In contrast, in the disordered case, there is a wide intermediate temperature range for which the typical $\{\sigma, \tau\}$ configurations form a hollow square shape, indicative of one Ising variable acquiring a finite value while the other one explores its entire configuration axis. Compared to the four sharp $\{\sigma, \tau\}$ peaks of the clean case, these enhanced correlations also cause an unexpected increase of the magnetic susceptibility in the disordered system. The nematic susceptibility, on the other hand, is always suppressed with respect to the clean case. This is not the only effect of random strain on the magnetic and nematic susceptibility: while their peaks are coincident in the clean case, they split in the disordered case.

Moreover, nontrivial magnetic correlations also appear in time domain. In the clean case, the two magnetic variables fluctuate in a nearly independent fashion, and the corresponding power spectral densities display a low-frequency plateau. On the other hand, in the disordered case, the magnetic fluctuations are correlated, in that if one of the Ising variables fluctuates around a nonzero value, the other one must fluctuate around zero. This results in coherent switching events and in power spectral densities that show no plateau behavior up to the very low frequencies probed in our simulations. Finally, we discuss possible experimental manifestations of the various random strain induced effects on the magnetic degrees of freedom.

The structure of this paper is as follows. We first motivate and introduce the RBFM in Sec. II, as well as discuss some of its qualitative properties in two dimensions. In Sec. III, we introduce our main replica-exchange WL simulation and discuss the disorder-averaged thermodynamic behavior seen in the RBFM. Additionally, we compare our results for the RBFM to our simulations of the RFIM. Following this, in Sec. IV, we discuss the time dependence of the fluctuations in the RBFM when we impose relaxational dynamics on the system. Finally, we summarize and discuss the implications of our results in Sec. V. Appendix A derives the low-energy mapping that gives rise to our RBFM, and Appendix B presents the technical details of our Monte Carlo simulations.

II. RANDOM BAXTER-FIELD ASHKIN-TELLER MODEL (RBFM)

A. Connection with the iron pnictides and the J_1-J_2 model

The low-energy properties of the magnetic and nematic phases of the iron pnictides are often described by means of the J_1-J_2 model [36,37,39,49]. The J_1-J_2 Hamiltonian is given by

$$H = J_1 \sum_{\langle ij\rangle} \mathbf{S}_i \cdot \mathbf{S}_j + J_2 \sum_{\langle\langle ij\rangle\rangle} \mathbf{S}_i \cdot \mathbf{S}_j, \tag{2}$$

where $\langle ij\rangle$ and $\langle\langle ij\rangle\rangle$ denote nearest-neighbor and next-nearest-neighbor sites i and j, respectively. The spins $\{\mathbf{S}_i\}$ are classical O(n) vectors that sit on a square lattice and interact with each other via the nearest-neighbor and next-nearest-neighbor exchange interactions J_1 and J_2.

Because the iron-pnictide compounds are metallic, the itinerant electrons play an important role, which is not captured by the J_1-J_2 model [40]. Nevertheless, the J_1-J_2 model can still be used as an effective low-energy model to gain insight into the magnetic and nematic properties of the iron pnictides. Indeed, the phase diagram of this model contains both a stripe-magnetic phase and a vestigial nematic phase [46].

While most studies in the pnictides have focused on the Heisenberg case ($n = 3$), the spins in these materials are typically confined to a single axis due to spin-orbit coupling [50,51]. Thus, hereafter we focus on the Ising limit ($n = 1$). The fourfold-degenerate ground state for the Ising case, shown in Fig. 1, consists of spin-up and spin-down stripes oriented parallel to either the x axis or the y axis.

To understand this degeneracy, we note that in the J_1-J_2 model applied to iron pnictides, the next-nearest-neighbor exchange J_2 is always antiferromagnetic while the nearest-neighbor exchange J_1 can be generally antiferromagnetic or ferromagnetic, When $J_2/|J_1| = 0$, the ground state is either Néel antiferromagnetic or ferromagnetic depending on whether $J_1 > 0$ or $J_1 < 0$, respectively. In the opposite limit, when $J_2/|J_1| \to \infty$, the ground state is stripe antiferromagnetic as the next-nearest-neighboring spins favor antiferromagnetic alignment, rendering the nearest neighbors on the two interpenetrating sublattices shown in Fig. 1 independent of one another.[1] When J_2 and $|J_1|$ are comparable, there is competition between the J_1 and J_2 terms, as the J_1 term favors *ferromagnetic* alignment of next-nearest-neighboring spins, whereas the J_2 term prefers these neighbors to have *antiferromagnetic* alignment. For this reason, the model is said to be frustrated.

The transition from the Néel or ferromagnetic ground state to the stripe-ordered ground state occurs at $J_2/|J_1| = \frac{1}{2}$. We therefore focus on the range $J_2/|J_1| > \frac{1}{2}$. In this regime, the Hamiltonian in Eq. (1) can be written as two antiferromagnetic Ising models on the A and B sublattices of the square lattice coupled by the J_1 term. Therefore, the stripe-magnetic order parameter has two components comprised of the staggered sublattice magnetizations, given by

$$M_{A,B} = \sum_{(i_x,i_y)\in A,B}^{N_S} (-1)^{i_x+i_y} S_i. \tag{3}$$

In the equation above, the summation runs over (i_x, i_y) integer pairs that index the sites that lie in either the A or B sublattice, each containing half of the total number of spins ($N_S = N/2$).

The nematic order parameter $\phi \propto M_A M_B$ is composite in terms of the primary magnetic order parameters M_i. It is Ising nematic because the sublattice magnetizations can be either aligned ($\phi > 0$) or antialigned ($\phi < 0$). These two cases represent the horizontal ($\phi > 0$) and vertical ($\phi < 0$) stripe configurations, as shown in Fig. 1. In the Ising J_1-J_2 model [48], long-range nematic order appears simultaneously with the primary stripe-magnetic phase, i.e., there is no separate nematic phase.[2]

---

[1] While in the Ising case the spins are collinear by construction, for O($n > 1$) realizations of the J_1-J_2 model, fluctuations give rise to a biquadratic term in the Hamiltonian that lock the staggered magnetizations of the two sublattices to be collinear [46], giving rise to a stripe-magnetic state similar to that in Fig. 1.

[2] In the J_1-J_2 model with classical vector spins, there is generally a nematic phase between the high-temperature paramagnetic phase and the ground-state stripe-magnetic phase [37,40]. This phase is characterized as one with $\langle \mathbf{M}_A \cdot \mathbf{M}_B\rangle \neq 0$ despite that $\langle \mathbf{M}_A\rangle = \langle \mathbf{M}_B\rangle = 0$. In purely two-dimensional systems, the stripe-magnetic phase only exists at $T = 0$ by the Mermin-Wagner theorem. However, the

The stripe configurations lower the tetragonal symmetry of the lattice to orthorhombic since bonds along the x axis connect parallel (antiparallel) spins, whereas bonds along the y axis connect antiparallel (parallel) spins. Due to magnetoelastic coupling, the nematic order parameter couples bilinearly to strain ε in the Ginzburg-Landau free energy $\varepsilon\phi \propto \varepsilon(M_A M_B)$ [13–15]. Here, the strain takes on the form

$$\varepsilon \equiv \partial_x u_x - \partial_y u_y, \tag{4}$$

with $\boldsymbol{u} = (u_x, u_y)$ denoting the lattice displacement.

B. Mapping onto the Ashkin-Teller model

While the Ising J_1-J_2 model captures the onset of coupled nematic and magnetic orders, this model's inherent frustration between the nearest- and next-nearest-neighboring interactions makes it difficult to be simulated numerically in the presence of disorder. Given that we are ultimately interested in understanding the effects caused by random disorder, which introduces its own set of frustrated interactions, we make use of a low-energy mapping that exists between the Ising J_1-J_2 model and the Ashkin-Teller model, the latter of which experiences no frustration in the absence of disorder.

The existence of a fourfold-degenerate ground state suggests that the properties of the Ising J_1-J_2 model may be captured by a model with Z_4 symmetry. That this is indeed the case was shown in Refs. [47,48], which numerically determined the phase diagram of the Ising J_1-J_2 model. It was found that for $\frac{1}{2} < J_2/|J_1| \lesssim 0.67$, there is a first-order transition from a paramagnetic phase into a stripe phase, whereas for $J_2/|J_1| \gtrsim 0.67$, the system undergoes a single second-order phase transition. Moreover, in the $J_2/|J_1| \to \infty$ limit, the transition is in the Ising universality class, whereas for $J_2/|J_1| \approx 0.67$, the transition has the four-state Potts universality. These two points are connected by a line of second-order transitions that displays *weak universality*, i.e., only the anomalous exponent $\eta = \frac{1}{4}$ is universal while the others depend on the ratio $J_2/|J_1|$ [47,48,52].[3] This is the same behavior displayed by the 2D Ashkin-Teller model (ATM), which is defined by

$$H_0 = -\sum_{\langle ij\rangle} [J(\sigma_i\sigma_j + \tau_i\tau_j) + K\sigma_i\tau_i\sigma_j\tau_j]. \tag{5}$$

In the expression above, there are two Ising spins at every site i, denoted by σ_i and τ_i. These spins are also known as the magnetic "colors" of the model. The Ising exchange J is ferromagnetic and the strength of the Baxter exchange coupling K represents the degree to which the two Ising magnetic colors are correlated. When $K = 0$, the model corresponds to two copies of the Ising model (like the Ising J_1-J_2 model when $J_2/|J_1| \to \infty$) whereas when $K = J$, it reduces to the four-state Potts model (like the Ising J_1-J_2 model when $J_2/|J_1| \approx 0.67$).

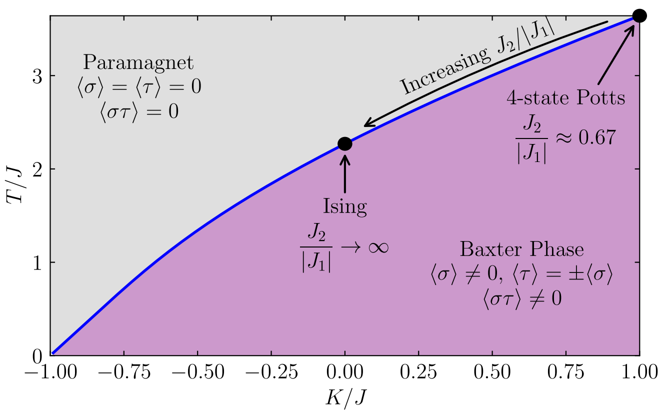

FIG. 2. Two-dimensional phase diagram of the Ashkin-Teller model along the temperature T and Baxter coupling K axes, according to Ref. [53]. A critical line separates the paramagnetic phase from the Baxter phase, along which only one critical exponent is universal. The points displaying Ising ($K = 0$) and four-state Potts ($K = J$) universality are indicated, as is the mapping of the Ising J_1-J_2 model with $J_2/|J_1| \gtrsim 0.67$ onto the $0 \leqslant K/J \leqslant 1$ region of the phase diagram established in Refs. [47,48].

In fact, the results of Refs. [47,48] established a one-to-one correspondence between the ATM with $0 \leqslant K/J \leqslant 1$ and the Ising J_1-J_2 model with $J_2/|J_1| \gtrsim 0.67$, such that $K = 0$ corresponds to $J_2/|J_1| \to \infty$ and $K = J$, to $J_2/|J_1| \approx 0.67$. The mapping takes on the following form:

$$\begin{aligned} \langle M_A\rangle &\quad\leftrightarrow\quad \langle\sigma\rangle, \\ \langle M_B\rangle &\quad\leftrightarrow\quad \langle\tau\rangle, \\ \langle\phi\rangle &\quad\leftrightarrow\quad \langle\sigma\tau\rangle. \end{aligned} \tag{6}$$

and is shown in Fig. 2 superimposed to the $(K/J,\ T/J)$ phase diagram of the ATM [53]. Along the interval $K/J \in (-1, 1]$, the ground state of the ATM is fourfold degenerate, and the system cools from a high-temperature paramagnetic phase, characterized by $\langle\sigma\rangle = \langle\tau\rangle = \langle\sigma\tau\rangle = 0$, into the so-called Baxter phase, which displays ferromagnetic order in both σ and τ such that $\langle\sigma\rangle = \pm\langle\tau\rangle$. Note that the Baxter phase also displays ferrolike order in the composite Baxter variable $\langle\sigma\tau\rangle$, which corresponds to the nematic order parameter of the Ising J_1-J_2 model. Therefore, in this model, the nematic (i.e., Baxter) and magnetic transitions happen simultaneously via a second-order transition. This is quite different from the large-n solution of the O(n) J_1-J_2 model, in which the two transitions are either split or simultaneous and first order [37,40]. The critical line separating the paramagnetic and Baxter phases is known exactly [48]:

$$\sinh\left(\frac{2J}{T_c}\right) = \exp\left(-\frac{2K}{T_c}\right). \tag{7}$$

As discussed above, along this line, only the anomalous exponent is universal, $\eta = \frac{1}{4}$, while the values of the other exponents (except for the exponent δ, given by $\delta = \frac{d+2-\eta}{d-2+\eta} = 15$) depend on the ratio K/J. We note that ordered phases exist outside the interval $K/J \in [-1, 1]$ [53]. For instance, the Baxter phase for $K/J > 1$ is preceded by a phase in

---

nematic order persists at finite temperature since it breaks a discrete symmetry instead of a continuous one.

[3] The conjugate field exponent δ is also universal for systems that exhibit weak universality, but one can think of it as being fixed by its relation to the anomalous exponent through hyperscaling.

which $\langle\sigma\tau\rangle \neq 0$ while $\langle\sigma\rangle = \langle\tau\rangle = 0$. Such a behavior is not observed in the Ising J_1-J_2 model. Hereafter, we focus only on the regime $K/J \in (0, 1)$ of the ATM, as it maps onto the $J_2/|J_1| \gtrsim 0.67$ regime of the Ising J_1-J_2 model.

C. Random strain and the emergence of two length scales

The role that structural disorder plays on the intertwined magnetic and nematic phases represents a new type of quenched disorder in statistical physics. Random strains in the lattice appear as a random-field disorder for the composite nematic degrees of freedom, whereas they appear as a random-bond disorder for the primary magnetic degrees of freedom. Typically, random-field disorder is more acute than random-bond disorder. Indeed, even a weak random field locally breaks symmetries of the Hamiltonian and can lead to domain breakup at $T = 0$ [21]. On the other hand, the system's exchange constant may overcome the effects of a weak bond disorder [1,2,54]. Random strain disorder is different than either the pure random-field or the pure random-bond disorder because the interplay between the magnetic and nematic degrees of freedom allows for the two types of disorder effects to feed back onto each other.

Random strain disorder, denoted by the local variable ε_i, appears as an onsite term through the bilinear coupling to the Ising-nematic variable of the problem. For an isolated Ising-nematic instability, as discussed in Refs. [17–20], this results in the random-field Ising-model (RFIM). In the case of the ATM considered here, random strain disorder maps onto a *random Baxter field*, as the nematic order parameter is the composite $\sigma\tau$ (see Appendix A). This leads us to the *random Baxter-field Ashkin-Teller model* (RBFM), presented in Eq. (1) and repeated here for convenience:

$$H = -\sum_{\langle ij\rangle}[J(\sigma_i\sigma_j + \tau_i\tau_j) + K\sigma_i\tau_i\sigma_j\tau_j] - \sum_i \varepsilon_i\sigma_i\tau_i. \quad (8)$$

In our simulations, disorder is taken to be spatially uncorrelated and sampled from a box distribution:

$$\rho(\varepsilon_i) = \begin{cases} \frac{1}{4\varepsilon}, & \varepsilon_i \in [-2\varepsilon, 2\varepsilon] \\ 0, & \text{otherwise.} \end{cases} \quad (9)$$

Consequently, ε denotes the typical disorder strength. We note that while the disorder term in Eq. (8) acts only as a random field for the Baxter variable $\sigma\tau$, a random-bond term is generated by fluctuations (e.g., in the renormalization-group flow) for the individual magnetic variables σ and τ. Thus, the RBFM captures the feedback that exists between the random-field and random-bond effects promoted by random strain disorder in the iron pnictides.

Following the Imry-Ma-Binder analysis [21,22], the Baxter phase of the clean 2D ATM, subject to the random Baxter field in Eq. (8), will break apart into domains even at $T = 0$. The length scale at which this occurs is given by the breakup length

$$\ell_b \sim \exp\left[C\left(\frac{J+K}{\varepsilon}\right)^2\right], \quad (10)$$

that grows exponentially with the ratio between the "total" exchange and the disorder strength. In the expression above, C is a constant of order one. Thus, we do not expect long-range order at any temperature in the thermodynamic limit.

Because the random Baxter field acts on an Ising composite variable, the domain breakup occurs specifically for the composite variable. This means domain walls form when the product $\sigma\tau$ changes value. This is achieved when either σ or τ changes value, *but not if both do.* At first sight, this seems to imply that one magnetic order parameter could maintain long-range order while the other one breaks up to satisfy the constraints of the random Baxter field. However, such a state is degenerate with one where both orders eventually break apart, resulting in magnetic domain breakup as well. Thus, all long-range order is lost in the RBFM at $T = 0$. While we argue that the domain breakup occurs for the RBFM, we note that nematic, and therefore magnetic, domain breakup was also seen in the diluted Ising J_1-J_2 model in Refs. [55,56], due to the same low-energy physics created by the random strain disorder.

What makes this model display a richer and more complex behavior than the RFIM is the fact that disorder introduces nontrivial correlations between σ and τ. Consider, for example, the sizes of the magnetic domains compared to the nematic domains. In the RFIM, a single disorder configuration should fix the ground-state configuration [57]. In the RBFM, meanwhile, because only one of the two magnetic variables can change at a time across a nematic domain wall, the typical breakup size of the magnetic domains is larger than the nematic domains. This introduces a second breakup length scale into the problem, which is not seen in the RFIM.

Additionally, there is a potentially large degeneracy associated with the number of ways one can satisfy the disorder constraint with multiple magnetic domain configurations. This is sketched in Fig. 3, where we schematically show identical Baxter domain breakup associated two different σ and τ domain configurations. Therefore, these two different magnetic states are degenerate. The residual degeneracy expected in the ground state of the RBFM contrasts with that of the RFIM, which is expected to be unique [57]. This ground state degeneracy is attributed to the fact that, because disorder locally favors a value of the composite Baxter variable, it leaves intact a twofold symmetry of a system.

To assess the difference in domain breakup sizes more clearly, we show the results of an adaptive simulated annealing run of Eq. (8) for a system of linear size $L = 400$ with a final temperature of $T = 0.269\,J$, Baxter coupling $K = 0$, and a single disorder configuration with strength $\varepsilon = J$. Details of our simulated annealing regimen are given in Appendix B 1. The final spin values are plotted in Fig. 4, with the yellow (light) and blue (dark) regions representing Ising domains with value ±1. It is clear that the typical nematic domain size is smaller than the typical magnetic domain size.

To make a more quantitative comparison, the spin autocorrelation functions $\mathcal{A}$ for various temperatures during the simulated annealing regimen are shown in Fig. 5. This quantity is defined by

$$\mathcal{A}[\sigma; r] \equiv \text{Av}\left\{\frac{1}{L^2}\sum_{\boldsymbol{x}}(\sigma_{\boldsymbol{r}+\boldsymbol{x}} - \overline{\sigma})(\sigma_{\boldsymbol{x}} - \overline{\sigma})\right\}_{r\leqslant|\boldsymbol{r}|<r+1} \quad (11)$$

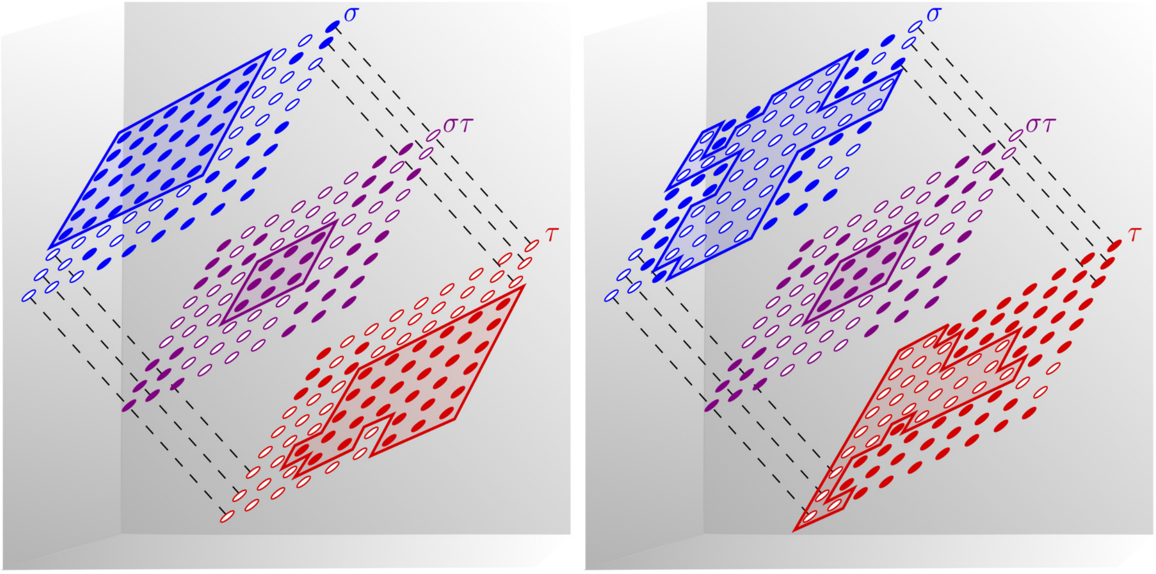

FIG. 3. Each random Baxter-field configuration fixes a Baxter domain configuration, as shown in the central view of the two-dimensional lattice in this sketch (purple). In both panels, the Baxter ($\sigma\tau$) domain configuration is identical, but the magnetic domains σ (red) and τ (blue) are different, as shown by the top and bottom views, respectively.

for the σ field, where $\boldsymbol{r} = r(\cos\theta, \sin\theta)$ and $\overline{\sigma}$ is the net σ-magnetic moment per site. The notation $\mathrm{Av}\{Q\}_\varsigma$ denotes an average over the values of the quantity Q that satisfy condition ς. Similar expressions hold for $\mathcal{A}[\tau; r]$ and $\mathcal{A}[\sigma\tau; r]$. The autocorrelation functions are nearly linear at short distances in the linear-logarithm plot of Fig. 5, indicating that $\mathcal{A}(r) \sim e^{-r/R}$ for small distances r. The vertical dashed lines denote the distances R where the spin autocorrelation functions equal e^{-1} at the lowest temperature measured, corresponding to the domains shown in Fig. 4. It is clear that $R_{\sigma\tau}$ is a factor of 2–3 smaller than R_σ, R_τ. Interestingly, as the system is annealed and the thermal fluctuations are frozen out, the autocorrelation functions gradually approach the lowest-temperature values, indicating the existence of temperature-independent length scales for the Baxter and magnetic variables. These results, although typical, are for a single disorder configuration. In what follows, we quantitatively study the thermodynamics and relaxational dynamics of the RBFM after averaging over many different disorder configurations.

III. THERMODYNAMICS OF THE RANDOM BAXTER-FIELD ASHKIN-TELLER MODEL

A. Simulation and observables

We performed replica-exchange Wang-Landau (WL) Monte Carlo simulations to obtain the thermodynamics of the RBFM defined in Eq. (8). This method of simulation, as opposed to the Metropolis, heat-bath, or cluster algo-

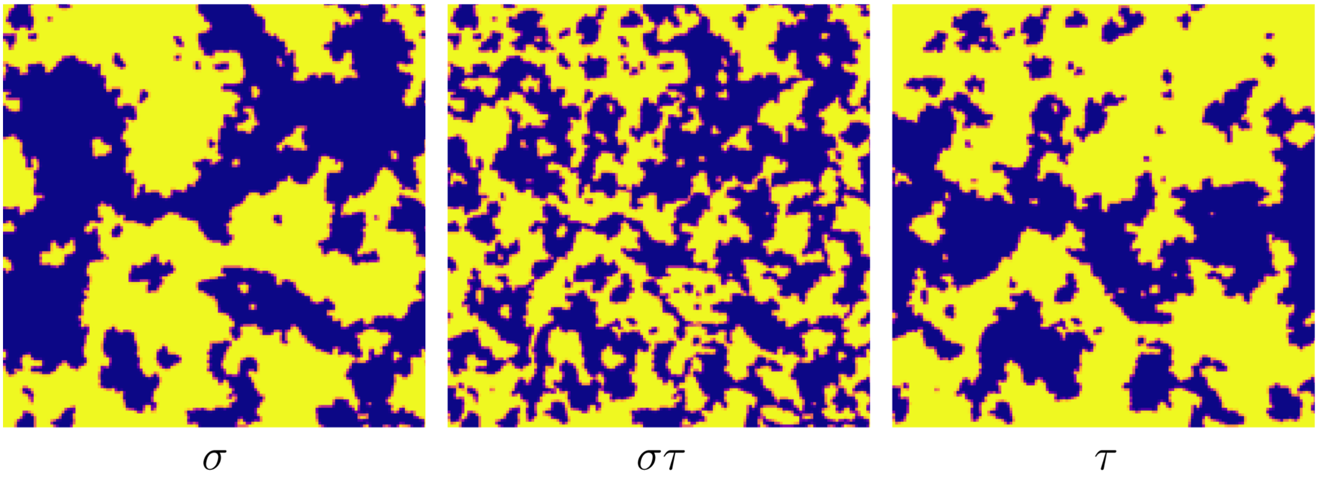

FIG. 4. Snapshots of the low-temperature domain structure generated by a simulated annealing run of Eq. (8) for a single disorder configuration with $K = 0$, $\varepsilon = J$, and $L = 400$. The Baxter domains in the $\sigma\tau$ panel are seen to be typically smaller than the magnetic domains in the σ and τ panels. The yellow (light) regions are those for which the field values are $+1$, whereas the blue (dark) regions correspond to -1. The red lines highlight the domain walls.

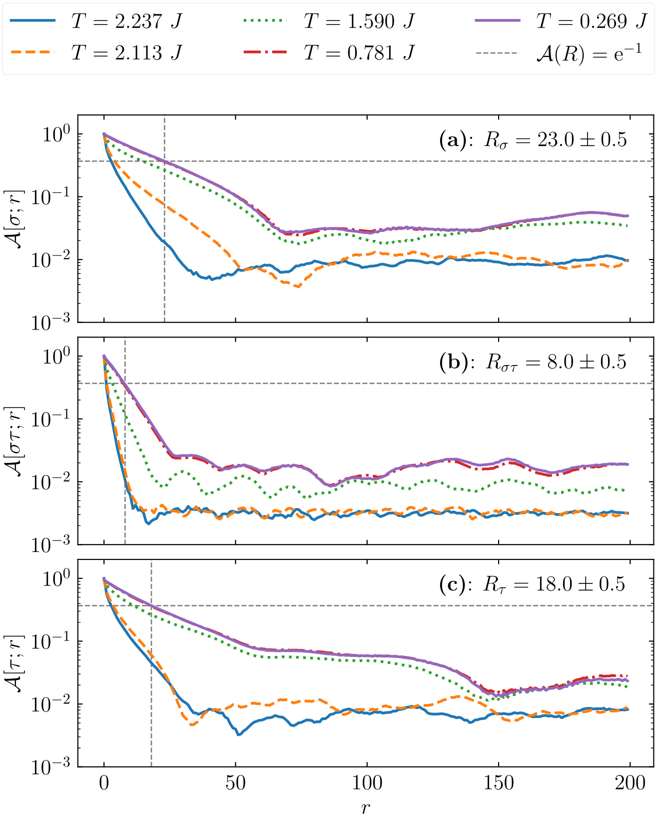

FIG. 5. Isotropic spin autocorrelation functions $\mathcal{A}(r)$ of snapshots of the spin configurations taken after equilibration at various temperatures during simulated annealing. These autocorrelations are of the (a) σ, (b) Baxter $\sigma\tau$, and (c) τ degrees of freedom and are measured with respect to the radial coordinate $r = \sqrt{x^2 + y^2}$. The vertical lines are positioned at the radius R where $\mathcal{A}(R) = e^{-1}$ at the lowest temperature probed.

rithms, circumvents slowing down near critical points and at low temperatures. Both the Metropolis and heat-bath algorithms suffer from critical (supercritical) slowing down near second-order (first-order) transitions due to the diverging correlation lengths (phase coexistence). Cluster algorithms, on the other hand, are not suitable for problems with random-field disorder. The WL algorithm is a temperature-independent approach that computes the microcanonical density of states [58,59]. Thermodynamic quantities can be obtained directly from the density of states. As a result, because temperature is not involved, the WL algorithm is free from critical or supercritical slowing down.

We employ the massively parallel replica-exchange WL algorithm to help the simulations converge in the presence of a rugged energy landscape [60–62]. The details of the algorithm are given in Appendix B. After the thermodynamic properties from each disorder configuration are obtained, we average over all configurations to obtain the mean value and standard errors for each observable.

Our analysis focuses on the specific-heat and uniform susceptibilities. We are primarily interested in measurements at a fixed system size of $L = 40$ and two different Baxter couplings: a finite Baxter value of $K = 0.5\,J$ and $K = 0$ (Ising-criticality point). We vary the random Baxter-field strength ε in Eq. (9) to study how the two different breakup length scales affect the disorder-averaged thermodynamics. All energy values are given in units of J and our results, when plotted as functions of temperature, are shown within one standard error represented by a shaded region about the mean. As thermodynamic quantities can be obtained rapidly from the simulated density of states for arbitrary temperatures within the WL procedure, we can achieve a high-temperature resolution. In most graphs, the temperature axis has a resolution of $0.001\,J$. When appropriate, the clean-system transition temperature calculated from Eq. (7) will be shown as well and denoted as $T_c^{(0)}$.

The specific heat for a single disorder configuration is calculated as

$$c_V = \frac{1}{NT^2}(\langle E^2\rangle - \langle E\rangle^2), \tag{12}$$

where E is the energy of the system, T is the temperature, $N = L^2$ is the total number of lattice sites, and $\langle\cdot\rangle$ represents a canonical thermodynamic average. Denoting the disorder average (see Appendix B 4 for details) with double brackets $[\![\cdot]\!]$, the disorder-averaged specific heat is then simply

$$[\![c_V]\!] = \frac{1}{NT^2}[\![\langle E^2\rangle - \langle E\rangle^2]\!]. \tag{13}$$

The number of disorder configurations averaged for each case ranges from 64 to 246; details are shown in Tables I and II in Appendix B 4.

There are four susceptibilities of interest in the problem: one for each magnetic variable σ and τ, one for the composite Baxter variable ϕ representing the nematicity, and one for the quadrature ζ of the two Ising variables. We define each of these quantities as

$$\sigma \equiv \frac{1}{N}\sum_{i=1}^{N}\sigma_i, \tag{14}$$

$$\tau \equiv \frac{1}{N}\sum_{i=1}^{N}\tau_{i,} \tag{15}$$

$$\phi \equiv \frac{1}{N}\sum_{i=1}^{N}\sigma_i\tau_i, \tag{16}$$

$$\zeta \equiv \sqrt{\sigma^2 + \tau^2}. \tag{17}$$

When there is no risk of confusion, we refer to the Baxter variable as $\sigma\tau$. Each of these observables has a uniform susceptibility given by

$$\chi_\alpha \equiv \frac{N}{T}(\langle\alpha^2\rangle - \langle|\alpha|\rangle^2) \tag{18}$$

for the observable α taken for a single disorder configuration. Disorder averaging follows the same approach as that for the specific heat.

B. Finite Baxter coupling

The specific-heat curves for an $L = 40$ and $K = 0.5\,J$ system and for different values of the disorder strength ε are shown in Fig. 6(a). The clean case ($\varepsilon = 0$) is shown for comparison. Increasing the disorder strength leads to a suppression

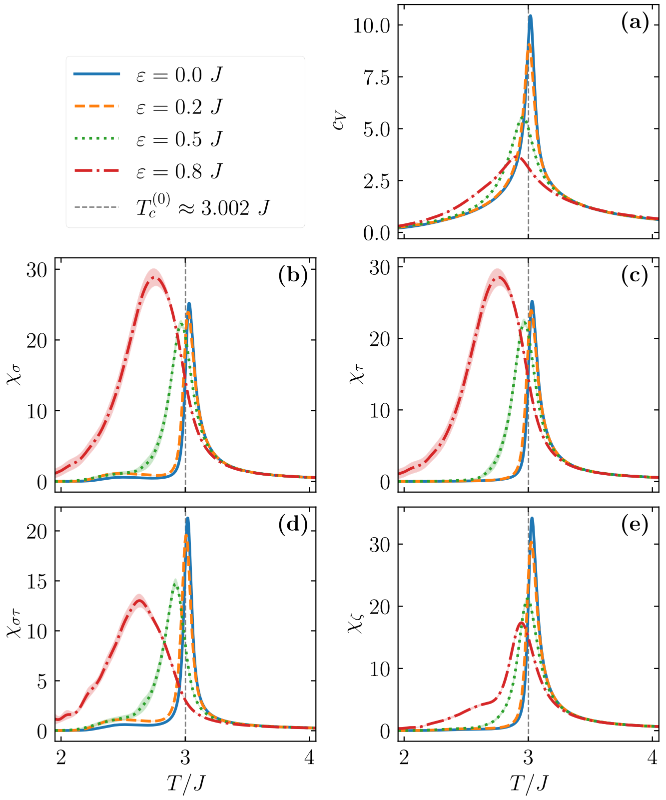

FIG. 6. Temperature dependence of (a) the specific-heat c_V and (b)–(e) the uniform susceptibilities of the RBFM for $K = 0.5\,J$ and linear size $L = 40$ at different disorder strengths ε. The susceptibilities are labeled as follows: (b) σ susceptibility χ_σ, (c) τ susceptibility χ_τ, (d) the Baxter susceptibility $\chi_{\sigma\tau}$, and (e) the quadrature susceptibility χ_ζ.

of the specific heat and to a shift in the peak position towards lower temperatures. These effects are due to the domain breakup length scale given by Eq. (10), which decreases with increasing disorder.

This behavior is confirmed by Fig. 7, which contrasts the specific-heat behavior between a clean and a disordered system with $\varepsilon = 0.5\,J$ as the system size L increases. The peak for the clean case increases and sharpens monotonically, with its position approaching $T_c^{(0)}$. Meanwhile, the peak in the disordered case saturates and shifts towards $T = 0$. This provides further evidence that the random Baxter field kills the thermodynamic phase transition of the clean ATM.

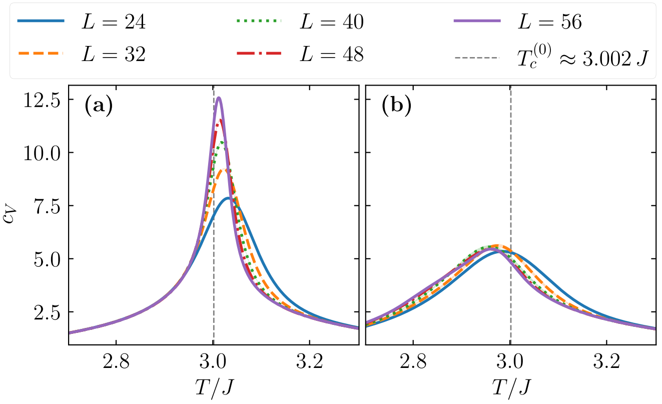

FIG. 7. Comparison of the specific heat c_V of (a) the clean system ($\varepsilon = 0$) and (b) the disordered system ($\varepsilon = 0.5\,J$) with increasing system size L. The Baxter coupling for both cases was set to $K = 0.5\,J$.

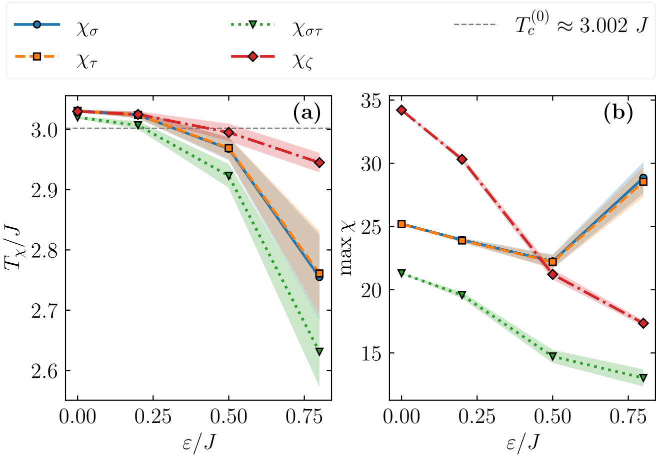

FIG. 8. (a) Peak susceptibility temperature T_χ and (b) peak susceptibility max χ as a function of disorder strength ε for $K = 0.5\,J$ and $L = 40$. The shaded regions represent T_χ and max χ to within a single error bar. The lines are guides to the eye.

Figures 6(b)–6(e) show the uniform susceptibilities for the observables defined in Eqs. (14)–(17). Like the specific heat, the Baxter susceptibility $\chi_{\sigma\tau}$ broadens and its peak is suppressed. A similar behavior is observed for the quadrature susceptibility χ_ζ. However, the peak in the two magnetic susceptibilities χ_σ and χ_τ are nonmonotonic functions of disorder. They actually increase for sufficiently large disorder strength, indicating an increase in the magnetic fluctuations due to the random Baxter field. The behavior of each susceptibility's peak value (max χ) and peak temperature (T_χ) is shown in Fig. 8 as a function of the disorder strength. We propose that the enhancement of max χ starts when the disorder strength reaches values for which the breakup length ℓ_b becomes comparable with or smaller than the system size L, such that the random Baxter-field effects become more pronounced. We will come back to this point in the next section.

In Figs. 9 and 10, we probe the (σ, τ) configurational space by showing the joint distribution of the two spin quantities σ and τ for both the clean case and the case with strong disorder ($\varepsilon = 0.5\,J$), respectively. These plots thus give the density of σ and τ fluctuations. The highest temperature in each figure (bottom right panel) was chosen to be the temperature where the magnetic susceptibilities in Fig. 6 start to separate ($T \approx 3.2\,J$). The temperatures are measured in units of the peak $\chi_{\sigma,\tau}$ temperature, which we denote by T_χ.

By comparing these figures, one sees that the distributions are nearly identical at high temperatures, consisting of broad peaks centered at the origin. However, upon cooling towards T_χ, the clean and disordered distributions behave very differently. In the clean case, the correlation between the σ and τ variables enforced by the Baxter exchange K results in peaks

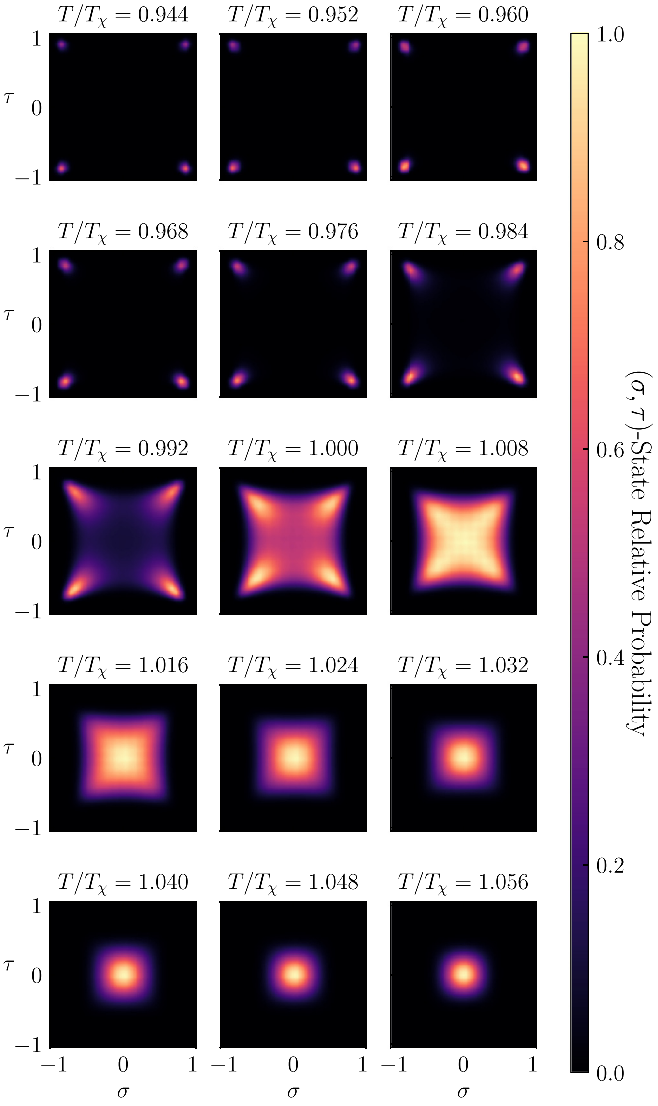

FIG. 9. Relative thermodynamic probabilities of (σ, τ) states for the clean case with $K = 0.5\,J$. The central temperature corresponds to the peak $\chi_{\sigma,\tau}$ position, $T_\chi = 3.031\,J$. The highest temperature is $T = 3.2\,J$.

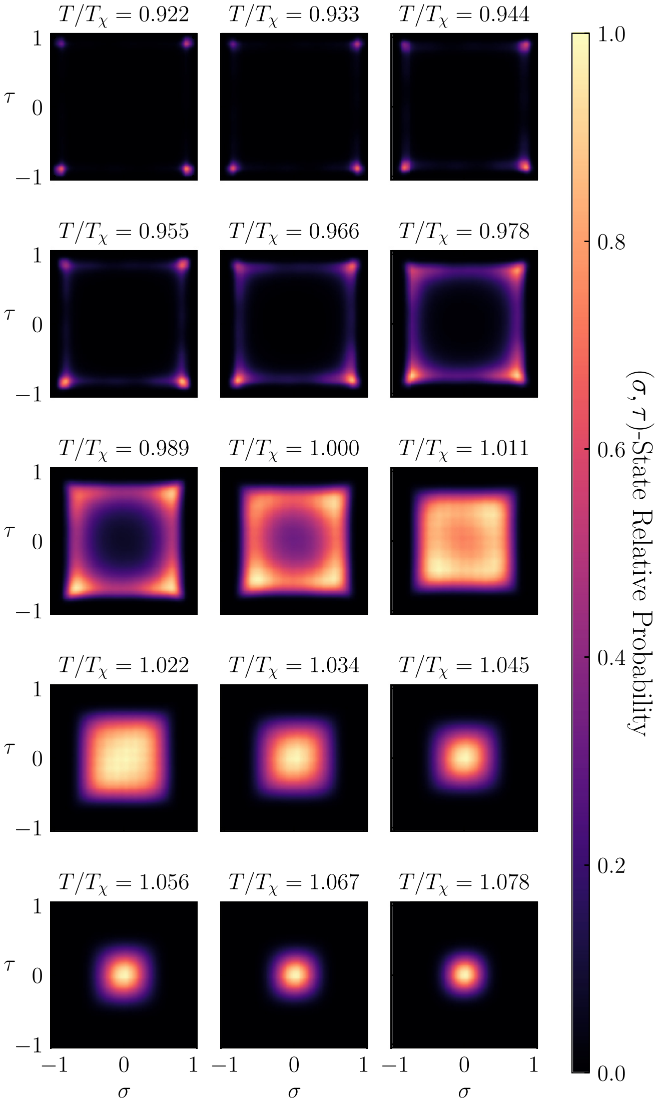

FIG. 10. Relative thermodynamic probabilities of (σ, τ) states with $K = 0.5\,J$ and a random Baxter-field strength of $\varepsilon = 0.5\,J$. The central temperature corresponds to the peak $\chi_{\sigma,\tau}$ position, $T_\chi = 2.968\,J$. The highest temperature is $T = 3.2\,J$, which is the same as Fig. 9.

along the diagonals in the (σ, τ) plane, which become sharper as the temperature is lowered. Meanwhile, in the disordered case, a nearly uniform box distribution appears, as shown in the $T = 1.022\,T_\chi$ panel. This indicates that the σ and τ variables are nearly uncorrelated since their joint distribution is a simple product of two uniform distributions in σ and τ. This can be interpreted as if the Baxter exchange is weakened by the random Baxter field, enlarging the symmetry of the magnetic fluctuations relative to the clean system. Moreover, it is consistent with the disorder-promoted enhancement of χ_σ and χ_τ in Fig. 6.

Upon lowering the temperature below T_χ, we see that in the clean case (Fig. 9), the magnetic variables cluster in four peaks corresponding to the four ground states of the ATM. In contrast, when the disorder is present (Fig. 10), a squarelike distribution emerges with empty states in its interior, as shown in the $T = 0.978T_\chi$ panel. Such a joint distribution cannot be described as the product of two independent distributions, like it could for the case of the uniform square. Instead, they correspond to uniform fluctuations of one of the magnetic variables while the other acquires a constant finite value. Therefore, the random Baxter field induces new correlations between σ and τ. The conclusion we draw from these thermodynamic probability distributions is that disorder increases the fluctuations of the magnetic degrees of freedom while correlating them in a distinct way as compared to the clean case.

C. Zero Baxter coupling

Our numerical results for systems of size $L = 40$ in Fig. 8(b) show that when the disorder strength becomes comparable to the Baxter exchange scale K/J, the magnetic fluctuations grow. To shed light on this result, and to disentangle the correlations between σ and τ induced by disorder

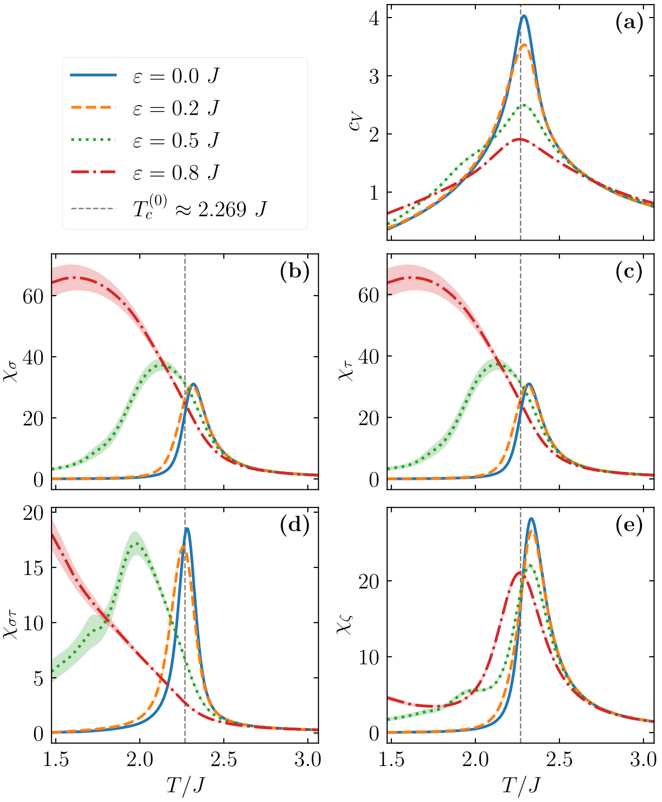

FIG. 11. Temperature dependence of (a) the specific-heat c_V and (b)–(e) the uniform susceptibilities (χ) of the RBFM for $K = 0$ and linear size $L = 40$ at different disorder strengths ε. The susceptibilities are labeled as follows: (b) σ susceptibility χ_σ, (c) τ susceptibility χ_τ, (d) the Baxter susceptibility $\chi_{\sigma\tau}$, and (e) the quadrature susceptibility χ_ζ.

(shown in Fig. 10) from the correlations enforced by K (shown in Fig. 9), we simulate the $K = 0$ RBFM. It corresponds to two clean Ising models coupled to each other only locally by the random Baxter field.

The specific heat for the RBFM with linear size $L = 40$ and $K = 0$ is shown in Fig. 11(a). While the specific-heat peak is suppressed with increasing disorder, it stays essentially at the clean transition temperature $T_c^{(0)}$ of the 2D Ising model. This contrasts with the $K = 0.5\,J$ case [Fig. 6(a)], where the peak position shifts to lower temperatures.

On the other hand, the uniform susceptibilities in Figs. 11(b)–11(e) for $K = 0$ show a qualitatively similar behavior with increasing disorder as they did for $K = 0.5\,J$. Quantitatively, however, the magnetic fluctuations overcome the clean-system susceptibility for smaller ε values, as shown in the plots of the susceptibility's peak value (max χ) and peak temperature (T_χ) in Fig. 12. This is consistent with the breakup length ℓ_b in Eq. (10) being suppressed in the $K = 0$ case, thus reaching the system's size L for smaller disorder strength values than in the $K = 0.5J$ case. We also note that, unlike the $K = 0.5\,J$ case, the Baxter fluctuations eventually exceed the clean system's fluctuations at large enough disorder values.

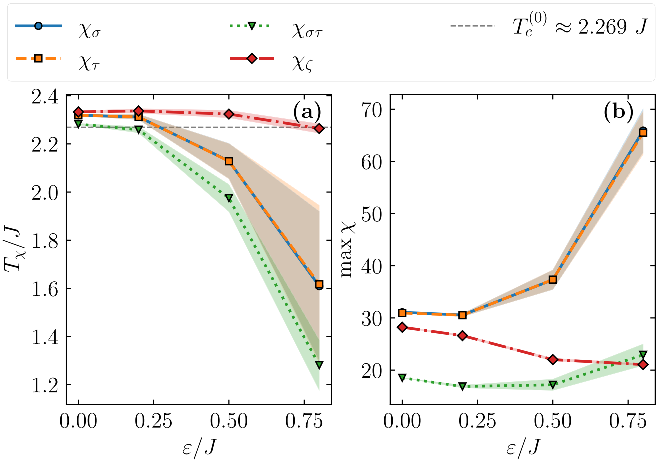

FIG. 12. (a) Peak susceptibility temperature T_χ, and (b) peak susceptibility max χ as a function of disorder strength ε for $K = 0$ and $L = 40$. The shaded regions represent T_χ and maxχ to within a single error bar. The lines are guides to the eye.

Figure 13 shows the relative thermodynamic probability of a (σ, τ) state for $K = 0$ and $\varepsilon = 0$, while the disordered case with $\varepsilon = 0.5\,J$ is shown in Fig. 14. The distribution at peak temperature $T/T_\chi = 1$ for the clean system in Fig. 13 is qualitatively similar to that in Fig. 10 for the disordered system with $K = \varepsilon = 0.5\,J$. Indeed, both cases show a lack of statistical weight near the paramagnetic state $(\sigma, \tau) = (0, 0)$. Moreover, at temperatures just above T_χ, both distributions have a nearly uniform-box structure, indicating that σ and τ are nearly uncorrelated. These comparisons support the notion that the random Baxter field effectively renormalizes the finite Baxter coupling down.

This is not the only effect of the random Baxter field. Comparing Fig. 14, which refers to the disordered system ($K = 0$, $\varepsilon = 0.5\,J$), with Fig. 10, which refers to the disordered system with finite Baxter coupling ($K = 0.5\,J$, $\varepsilon = 0.5\,J$), the emergence of disorder-induced correlations between σ and τ near T_χ is much more transparent in the former. Specifically, as the system cools down from the high-temperature paramagnetic phase, the statistical weight moves radially away from the paramagnetic state and eventually forms a hollow squarelike shape, which is sharper than the similar hollow-square shape in Fig. 10 for $K = 0.5\,J$. Once again, this squarelike joint distribution cannot be factorized into two separate distributions of σ and τ, and it is absent completely in the clean case with $K = 0$. This means that the random Baxter field introduces correlations between the magnetic variables. Along each side of the squarelike distribution, one of the magnetic variables is fixed at some value, while the other thermally fluctuates. This behavior satisfies the random Baxter-field constraint imposing nematic domain breakup along each side of the squarelike distribution. For example, along the upper and lower sides of the square, the average of the $\sigma\tau$ order parameter vanishes because the average σ order parameter does, despite the fact that the average τ order parameter does not.

D. Comparison with the random-field Ising model

As discussed in the Introduction, while the RBFM describes the impact of random strain on composite nematicity

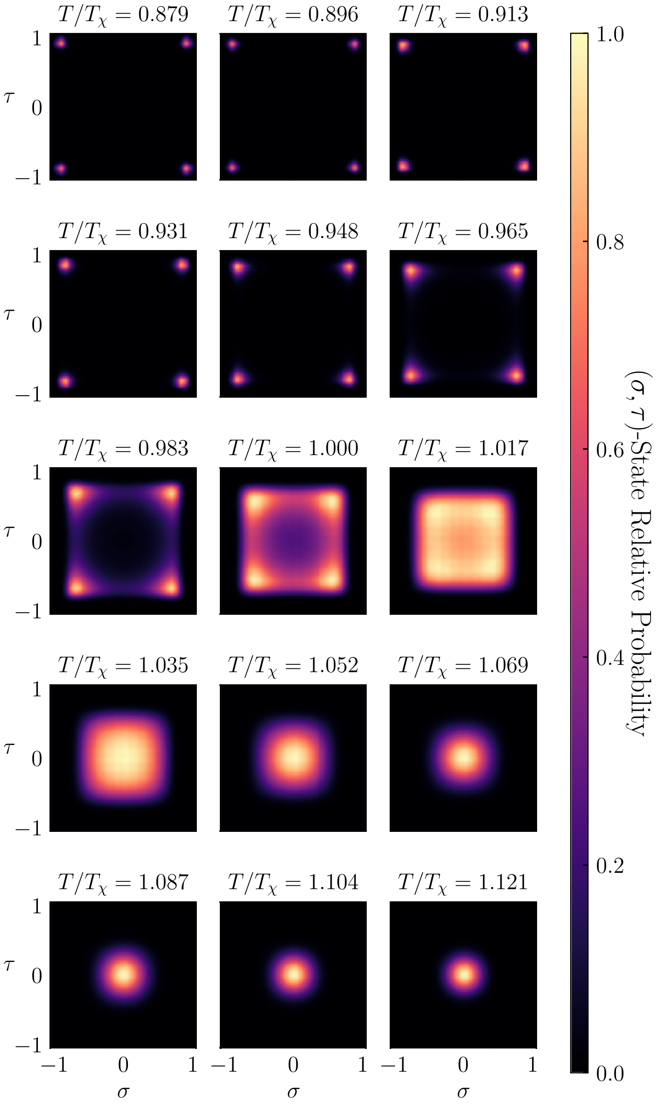

FIG. 13. Relative thermodynamic probabilities of (σ, τ) states for the clean case for $K = 0$. The central temperature corresponds to the peak $\chi_{\sigma,\tau}$ position, $T_\chi = 2.319J$. The highest temperature is $T = 2.6J$.

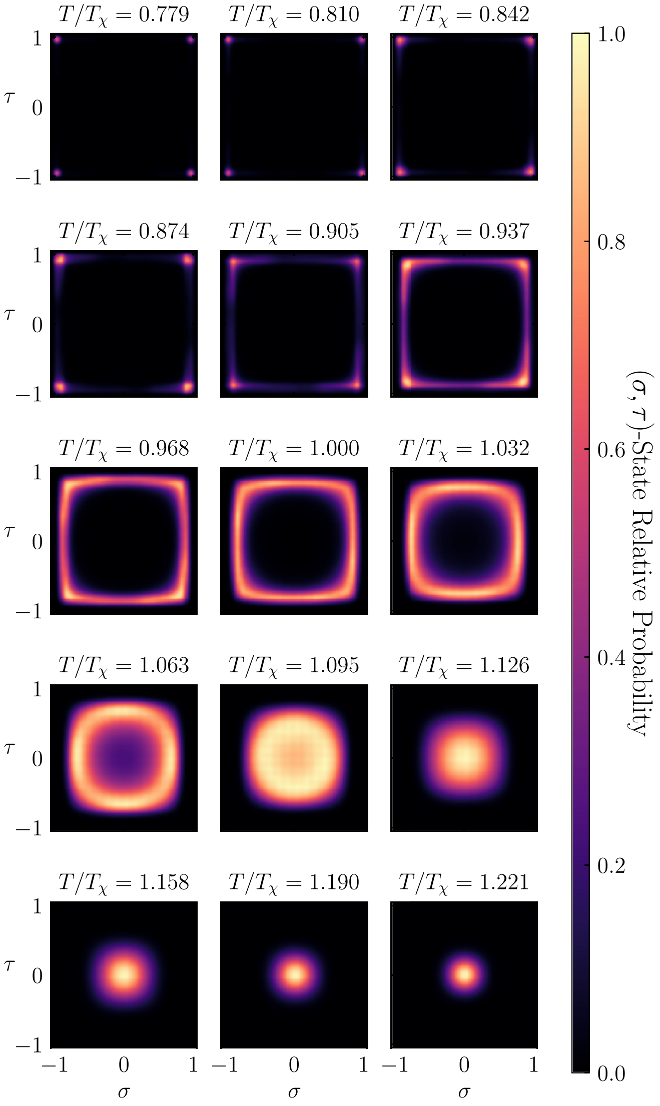

FIG. 14. Relative thermodynamic probabilities of (σ, τ) states for $K = 0$ with $\varepsilon = 0.5J$. The central temperature corresponds to the peak $\chi_{\sigma,\tau}$ position, $T_\chi = 2.129J$. The highest temperature is $T = 2.6J$ as it is in Fig. 13.

arising from an underlying magnetic- and charge-stripe order, the RFIM provides a suitable framework to describe the case in which nematicity is a primary instability of the system. It is therefore valuable to compare the properties of the RBFM with those of the RFIM, particularly when $K = 0$, since in this case the clean version of the RBFM belongs to the Ising universality class, similarly to the clean version of the RFIM. On the one hand, the RBFM displays the hallmark feature of the RFIM: the breakup of long-range nematic order into nematic domains. On the other hand, some of the thermodynamic properties of the RBFM differ from those of the RFIM.

Consider, for instance, the specific heat and the magnetic susceptibility for an $L = 40$ RFIM shown in Fig. 15, which we obtained from our replica-exchange WL simulation. The peaks of both c_V and χ_σ are suppressed and the corresponding peak temperatures shift towards $T = 0$. In the RBFM for $K = 0$, as shown in Fig. 11, the only thermodynamic quantities that share qualitative similarities to those of the RFIM are the Baxter and quadrature susceptibilities ($\chi_{\sigma\tau}$ and χ_ζ). The magnetic susceptibilities (χ_σ and χ_τ) and, more importantly, the specific heat c_V are different. Thus, the disorder physics in the RBFM must include effects with no counterpart in the RFIM.

To further illuminate this issue, we rewrite the RBFM Hamiltonian in Eq. (8) in terms of the local Baxter Ising variable $\phi_i = \sigma_i\tau_i$:

$$H = -J\sum_{\langle ij\rangle}\sigma_i\sigma_j - K\sum_{\langle ij\rangle}\phi_i\phi_j - \sum_i \varepsilon_i\phi_i - J\sum_{\langle ij\rangle}\phi_i\phi_j\sigma_i\sigma_j. \tag{19}$$

Written in this way, the RBFM Hamiltonian takes the form of a clean Ising model (IM) in σ coupled to a RFIM in ϕ through a four-spin operator. It is this four-spin operator that creates the correlations in the magnetic variables and gives rise to

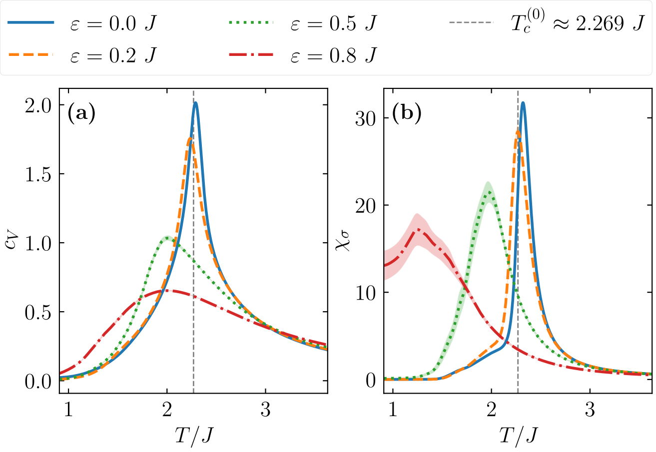

FIG. 15. Disorder-averaged thermodynamic quantities of the RFIM with linear size $L = 40$, measured as functions of temperature T, for various random-field strengths ε. (a) The specific heat c_V. (b) The magnetic susceptibility χ_σ.

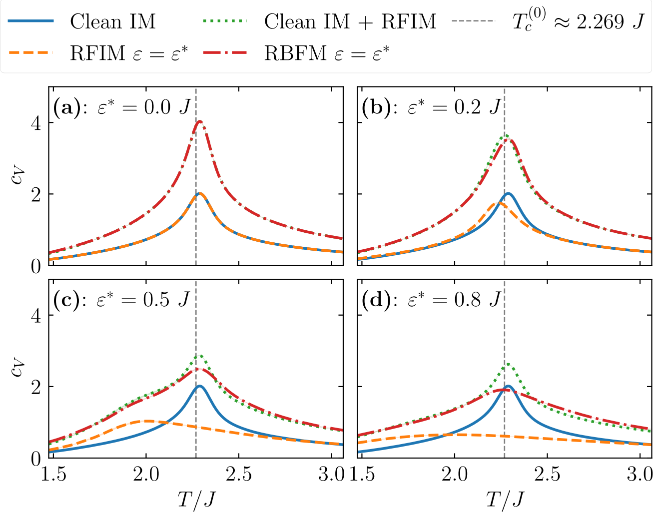

FIG. 16. Comparison of the RFIM and the RBFM with $L = 40$ and $K = 0$ over various disorder strengths. These plots show the specific heat c_V as a function of temperature T for the clean Ising model (clean IM); the RFIM at $\varepsilon = \varepsilon^*$, where ε^* is a numerical value defined in each figure; the sum of the specific heats of the clean IM and the RFIM (clean IM + RFIM); and the RBFM at zero Baxter coupling. (a) $\varepsilon^* = 0.0J$, (b) $\varepsilon^* = 0.2J$, (c) $\varepsilon^* = 0.5J$, and (d) $\varepsilon^* = 0.8J$. In the clean case (a), the Ashkin-Teller model is equivalent to two clean Ising models, as shown by the complete agreement between the green dotted curve and the red dashed-dotted curve.

effects beyond the RFIM. Such an operator is particularly interesting because it effectively generates a bond-dependent exchange for both the σ IM and the ϕ RFIM components of the RBFM. The effective σ exchange is given by $J_{ij}^{(\sigma)} \equiv -J(1 + \phi_i\phi_j)$ which is ferromagnetic when the bond connects Baxter variables in the same domain with $\phi_i\phi_j = 1$. However, when the bond is across a Baxter domain wall such that $\phi_i\phi_j = -1$, then $J_{ij}^{(\sigma)} = 0$, i.e., the magnetic degrees of freedom separated by this bond are independent. This again illustrates that domain breakup in the Baxter variable necessarily leads to domain breakup in the magnetic variables, and shows how the magnetic breakup length is larger than the Baxter one.

Conversely, the effective Baxter exchange is given by $J_{ij}^{(\phi)} \equiv -K - J\sigma_i\sigma_j$. Thus, if neighboring magnetic spins belong to the same domain with $\sigma_i\sigma_j = 1$, then the Ising Baxter degrees of freedom experience a ferromagnetic exchange. Meanwhile, if the neighboring magnetic spins are separated by a magnetic domain wall such that $\sigma_i\sigma_j = -1$, then the Ising Baxter degrees of freedom experience an antiferromagnetic exchange. This additional frustration for the Baxter variables leads to more breakup, providing a feedback mechanism on the composite degrees of freedom that is lacking in the conventional application of the RFIM. But these effects only become clear when both the ϕ and σ breakups are present.

To test this idea, Fig. 16 shows the evolution of the specific heat of the RBFM as the disorder strength is increased, and compares it to that of a clean IM, the RFIM, and the sum of the clean IM and the RFIM. For small disorder strengths, there is barely any Baxter domain breakup, which explains the small difference between the RBFM and the sum of the two Ising models. As the disorder strength increases, however, and domain breakup in both variables is more common, the splitting of the RBFM curve from the curves obtained from the sum of a clean IM and a RFIM becomes clearer. While some of the behavior of the RBFM specific heat is captured by the sum, such as the frozen peak temperature of the specific heat and the bump at low T, the suppression of the specific-heat peak is not. This suppression indeed highlights the role that the random Baxter field has in correlating the primary magnetic degrees of freedom in a way absent in the RFIM.

IV. RELAXATIONAL DYNAMICS OF THE RANDOM BAXTER-FIELD ASHKIN-TELLER MODEL

A. Dynamical simulation details

Our replica-exchange WL results reveal that for strong enough disorder, when the Baxter coupling is effectively suppressed, the two magnetic variables remain coupled to each other through the random Baxter field. As shown in Fig. 14, these disorder-induced correlations force only one magnetic variable to fluctuate at a time, enlarging the magnetic breakup lengths over the nematic one.

The two domain breakup length scales for the magnetic and Baxter domains should influence their dynamics as well. For example, if one were to assume relaxational domain dynamics of the Arrhenius law form, then the typical frequency of switching events would scale as $\exp(-\lambda\ell/T)$, where λ is the surface tension of a domain wall and ℓ is the domain size. Then, when two typical domain sizes exist in the problem, there should be two typical frequencies, with the faster arising from the smaller Baxter domains and the slower one from the larger magnetic domains. To verify this expectation, we simulate here random strain effects on the relaxational dynamics of the RBFM.

Metropolis Monte Carlo [63] simulations were run for the RBFM to simulate the relaxational dynamics of the magnetic fluctuations for the $K = 0$ case. The Metropolis algorithm simulates the dynamics of thermally activated excitations of equilibrium systems. We use the time records generated by the Metropolis Markov chains as a proxy of the time evolution of these excitations. This is justified if the model dynamics belongs to Hohenberg and Halperin's *Model A* classification [64,65]. Considering that the stripe-magnetic phase has a nonconserved order parameter, and that neither the magnetic nor the nematic order parameters are coupled to conserved quantities, the domain dynamics of the model is indeed expected to be relaxational and fall within the Model A classification.

The Monte Carlo timescale was set by a single sweep, defined by $2L^2$ single-spin Metropolis updates. A single Monte Carlo sweep then maps onto the shortest physical real-time scale of the problem. This is associated with the expected time it takes for a single Ising spin to flip from one projection to the other. We note that, in iron pnictides, the typical relaxational timescales observed in the nematic-magnetic phase are of the order of tens of picoseconds [66].

The clean system was simulated at the clean 2D Ising transition temperature $T = 2.269\,J$ while the disordered system's temperature was set to $T_\chi = 2.129\,J$ (see Figs. 12 and 14). These values were chosen to compare critical magnetic fluctuations in the clean system with the disorder-enhanced fluctuations of the RBFM.

The time records of σ, τ, $\sigma\tau$, and ζ were taken for clean ($\varepsilon = 0$) and disordered systems ($\varepsilon = 0.5\,J$) with $L = 80$ and $K = 0$. The disordered systems each had different quenched disorder configurations. Each Markov chain was thermalized for $2^{18} \approx 2.6 \times 10^5$ sweeps and then the time records were measured for $L_t = 2^{22} \approx 4.2 \times 10^6$ sweeps. The power spectral density (PSD) was averaged 100 times for the clean case and over 200 disorder configurations for the disordered one. For a given time record $x = x(t)$ with time average $\overline{x}$, the PSD is defined by

$$\mathcal{P}[x(t); f] \equiv \frac{1}{L_t}\tilde{x}^*(f)\tilde{x}(f) - \overline{x}^2 L_t \delta_{f,0}, \tag{20}$$

where f has units of frequency and $\tilde{x}(f)$ is the discrete Fourier transform of $x(t)$. The PSD above is the cosine transform of the autocorrelation function of $x(t)$ given by

$$\mathcal{A}[x(t); t] = \frac{1}{L_t}\int dt'\,[x(t+t')x(t')] - \overline{x}^2. \tag{21}$$

The PSD is therefore the spectrum of the fluctuations contained in the time record. For fast timescales (large frequencies), the PSDs typically have power-law behavior. Meanwhile, for timescales longer than the longest switching time in the time record (small frequencies), the PSDs typically saturate [67–69].

B. Dynamics at zero Baxter coupling

The time records for the magnetic, Baxter, and quadrature variables are shown in Figs. 17 and 18 for a clean and a disordered system, respectively. These time records are typical among different disorder configurations. Additionally, the averaged PSDs for each observable are shown in the same figures. The time records are only shown over about 250 000 Monte Carlo sweeps to make the switching events clearer.

The clean-case time records in Fig. 17 show multiple-state switching events with the longest timescale being about 100 000 Monte Carlo sweeps. This is reflected in the averaged PSDs in the same figure, which exhibit a plateau at a frequency scale of 10^{-5} sweeps^{-1}. Additionally, the switching of the two magnetic variables appears independent, and their averaged magnetic PSDs appear identical. This is consistent with the fact that the clean system with $K = 0$ corresponds to two independent Ising models. Since the Baxter variable $\sigma\tau$ and the quadrature variable fluctuate whenever either σ or τ fluctuate, the typical timescales associated with these variables are smaller, with the longest one being about 50 000 for the Baxter variable. This smaller timescale is seen in the Baxter PSD as well, as the plateau is shifted by about a factor of 2 along the frequency axis. The quadrature variable fluctuates the fastest when σ and τ are simultaneously near zero.

The corresponding time records and PSDs for the disordered system in Fig. 18 show that the Monte Carlo dynamics of the fluctuations are qualitatively different than they are for the clean case. The most obvious difference is that the amplitude of the Baxter fluctuations is reduced. Similarly, the relative change in the quadrature variable is typically smaller than that in the clean system (with the exception of an event occurring near 100 000 Monte Carlo sweeps). The reduction of the Baxter noise can be attributed to domain breakup within the system, whereas that for the quadrature fluctuations is due to how infrequently both magnetic variables vanish simultaneously.

The main difference between the clean and disordered cases is that magnetic fluctuations are correlated in the latter due to the random Baxter field. Consider, for example, the time records between about 25 000 and 170 000 Monte Carlo sweeps, as highlighted in the purple region in Fig. 18. During this time period, the σ-magnetic variable is mostly fluctuating around $\sigma = 0$ and the τ-magnetic variable is fluctuating around $\tau \approx 0.75$. But, for times preceding this interval, or those immediately following it, the magnetic variables change roles with σ fluctuating around a finite value and τ fluctuating around zero. These relatively long time periods in which one magnetic variable has a finite expectation value while the other is fluctuating around zero correspond precisely to the hollow-square distribution of (σ, τ) states shown in Fig. 14 at temperatures $T < 1.095\,T_\chi$. The event around 100 000 Monte Carlo sweeps, which substantially changes the quadrature variable, seems to correspond to a failed, simultaneous switching of σ and τ.

The differences in the time records of the clean and disordered cases are also manifested in the PSDs. In both cases, the Baxter and quadrature variables show a plateau within the accessible frequency range, indicative of the longest timescale associated with these fluctuations [67]. However, plateaus for the σ and τ magnetic are absent in the disordered case, in contrast with the clean system. Indeed, the magnetic PSDs display power-law behavior down to the smallest frequencies accessible in the disordered system. This behavior indicates that the longest timescale associated with the magnetic variables is too long and inaccessible during these simulations, and at least two orders of magnitude longer than the Baxter timescale.

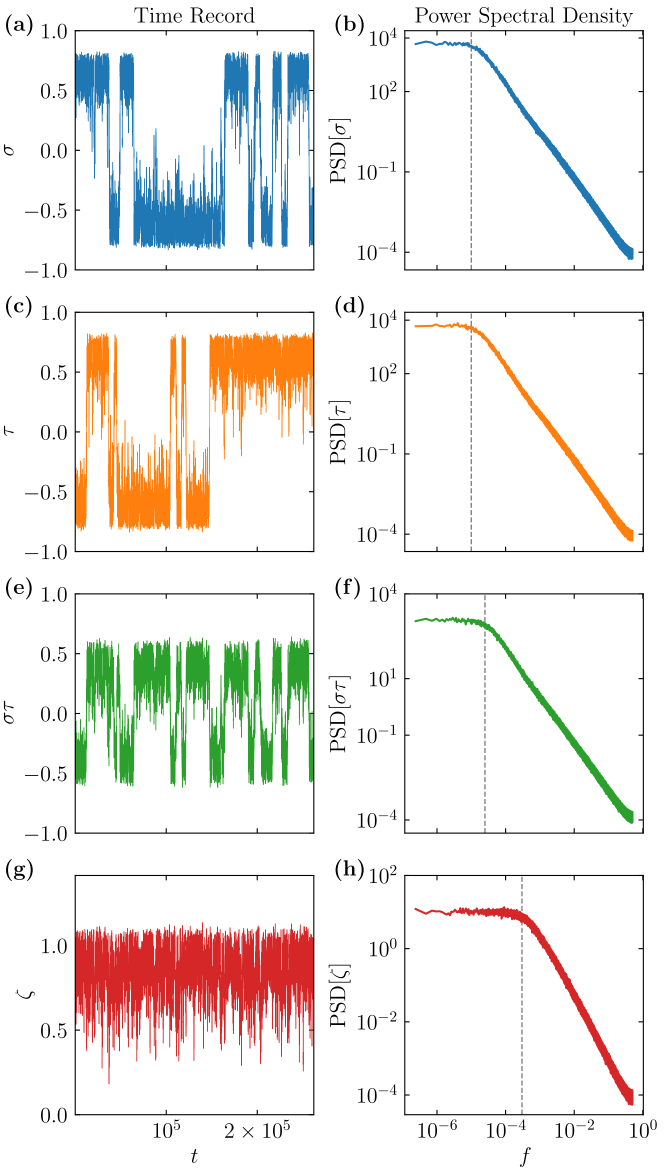

FIG. 17. Metropolis evolution of the RBFM for a system size $L = 80$ and $K = 0$ for the clean case ($\varepsilon = 0$) at the transition temperature $T_c^{(0)} \approx 2.269\,J$. We show a typical time record as a function of Monte Carlo sweeps t and the average power spectral density (PSD) as a function of frequency f for the (a), (b) σ, (c), (d) τ, (e), (f) Baxter $\sigma\tau$, and (g), (h) quadrature ζ variables. The vertical lines correspond approximately to the frequencies at which the PSDs cross over from a plateau to a power-law behavior.

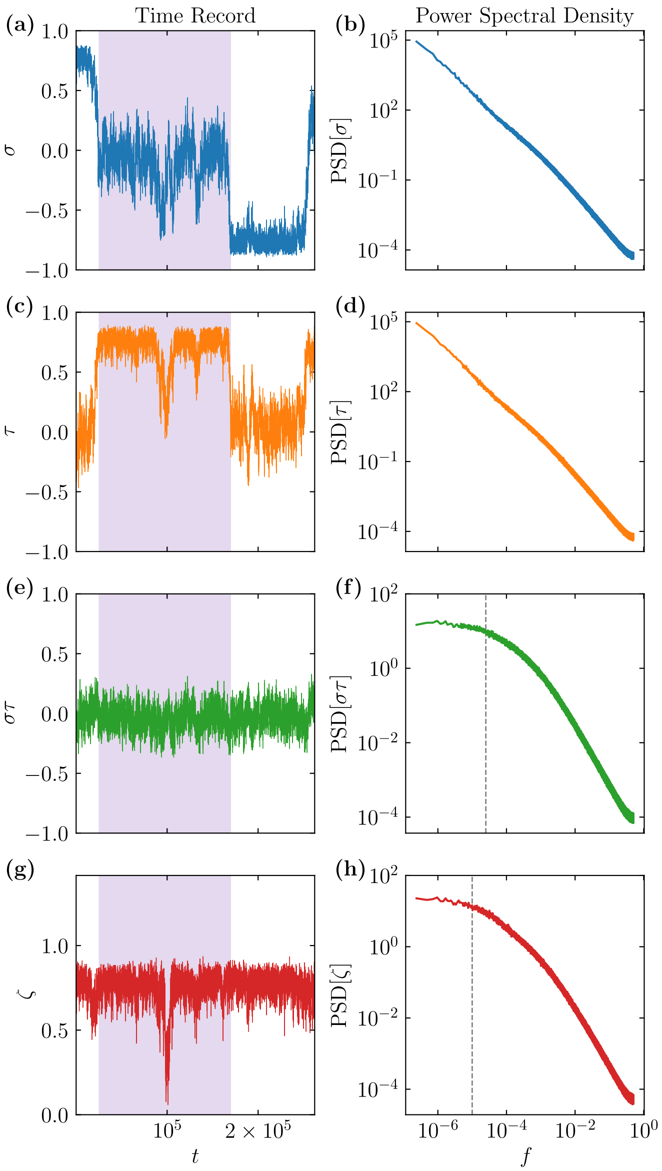

FIG. 18. Metropolis evolution of the RBFM for a system size $L = 80$, $K = 0$, and $\varepsilon = 0.5\,J$ at the peak temperature from Fig. 12 ($T_\chi = 2.129\,J$). We show a typical time record as a function of Monte Carlo sweeps t and the disorder-averaged power spectral density (PSD) as a function of frequency f for the (a), (b) σ, (c), (d) τ, (e), (f) Baxter $\sigma\tau$, and (g), (h) quadrature ζ variables. The vertical lines correspond approximately to the frequencies at which the PSDs cross over from a plateau to a power-law behavior, if plateaus are present. The highlighted region of the time records is discussed in the main text.

At first, one might have expected the Baxter and magnetic timescales to be comparable since the Baxter domains fluctuate only because the magnetic degrees of freedom fluctuate. Indeed, referring to the purple region in the time records of Fig. 18, the σ variable is fluctuating around zero, τ remains relatively constant, and the Baxter variable also fluctuates around zero. This shows that, overall, the σ variable is broken apart to satisfy the random strain constraint, allowing τ to take on a finite value. This would seemingly imply that the σ timescale should be comparable to the Baxter one, while the timescale for τ should be longer than both.

However, the event around 100 000 sweeps, in which there is a failure for σ and τ to switch roles, provides the explanation of why the magnetic timescales can be so much longer than the Baxter ones. While the Baxter variable fluctuates, the magnetic variables need to simultaneously break apart and reverse roles for a timescale to appear in the PSDs. But, such events are rare since the constraints imposed by the random Baxter field are satisfied by only a single magnetic variable. The scarcity of these events is what then leads to the long-time magnetic scales and to the disappearance of the plateaus in the magnetic PSDs.

V. DISCUSSION

The RBFM proposed and studied here provides a simple yet powerful framework to capture the impact of random strain in nematic systems for which the nematic instability is intertwined with a magnetic- (or charge-) stripe instability. Because in this case the nematic is a composite order parameter, random strain has a dual role as a random nematic field and a random magnetic bond. The extensive Monte Carlo simulations performed here reveal that, like in the RFIM, which is suitable for systems for which nematicity is a primary instability, the nematic ground state in the RBFM also breaks up in domains due to the random strain. However, in the RBFM, random strain also promotes correlations between the magnetic variables that have no counterpart either in the RFIM or in the clean Ashkin-Teller model. These correlations are ultimately a consequence of the fact that the constraints imposed by the random strain can be satisfied locally by two types of magnetic configurations, resulting in a residual degeneracy for the system. This property, in turn, is a direct manifestation of the composite character of the nematic order parameter.

We showed that these random strain promoted correlations are manifested in several properties of the RBFM. They not only promote the emergence of a second breakup length scale, but also of a second much longer timescale associated with the simultaneous switching of the two magnetic order parameters. These correlations appear unambiguously in the magnetic configurational space as a probability distribution of the $\{\sigma, \tau\}$ states in the shape of a hollow square. Such a distribution function is interpreted in terms of one magnetic Ising variable fluctuating around zero to satisfy the random strain constraint, while the other one acquires a nonzero average value. The main signature of the disorder-promoted correlations in the thermodynamics is the unexpected enhancement of the magnetic susceptibility for large enough disorder strength. In contrast, nematic fluctuations are generally suppressed by disorder, similarly to the RFIM.

The fact that multiple magnetic configurations can satisfy a given random strain realization suggests that, in contrast to the RFIM, the RBFM may have a macroscopic ground-state degeneracy. While our attempts to probe this macroscopic ground-state degeneracy via replica-exchange WL simulations gave inconclusive results, if this turns out to be the case, a spin-glass phase for the magnetic variables might emerge. Indeed, for the $K = 0$ case, the Hamiltonian in Eq. (8) has the form of two independent Ising models coupled by a random bond. This bilayer system is similar to the Edwards-Anderson (EA) model of spin glasses [70], although in this case, the two Ising layers representing the two magnetic variables in the RBFM would have clean Ising ferromagnetic exchanges within each layer, but the layers would be randomly coupled to each other locally due to random strain. It would be interesting to see if this EA implementation would also realize a low-temperature spin-glass phase characterized by replica-symmetry breaking [71].

The main material candidates to observe these effects are the iron pnictides of the 122 (e.g., $BaFe_2As_2$), 1111 (e.g., LaFeAsO), and 111 (e.g., NaFeAs) families. In all these cases, nematic order is intertwined with an antiferromagnetic stripe order, and there is strong evidence for the magnetic origin of the nematic instability [10]. In the language of the RBFM, onto which the Ising J_1-J_2 model can be mapped, the σ and τ variables refer to the staggered magnetizations of the two interpenetrating Néel sublattices that form the stripe state whereas the Baxter variable refers to the composite nematic order parameter (recall Fig. 1). In these and other materials, random strain is promoted by both chemical substitution and intrinsic lattice defects such as vacancies, interstitials, dislocations, and twin boundaries [72]. These intrinsic effects can be partially remedied via annealing, which was shown in $CaFe_2As_2$ to reduce the amount of random strain present in the sample [73]. Interestingly, in $BaFe_2As_2$, annealing was found to bring the magnetic and nematic transitions closer together towards a simultaneous first-order transition [74]. A similar reduction of the splitting between the two transitions was seen in CeFeAsO single crystals when compared to polycrystalline samples, which presumably have larger intrinsic random strain [75]. These observations, as well as the general increase of the magnetic transition temperature in annealed samples [73–75], are qualitatively consistent with the splitting between the peak temperatures of the magnetic and Baxter susceptibilities seen in our simulations (see Fig. 12). Of course, while in our 2D RBFM model no long-range order is allowed, the magnetic and nematic transitions are expected to survive up to a finite disorder strength in a more realistic model with coupled RBFM layers.

Evidence for inhomogeneous and glassylike fluctuations was reported by nuclear magnetic resonance (NMR) measurements in 1111 [76] and 122 compounds [77,78]. In the case of LaFeAsO, nuclear quadrupole resonance (NQR) measurements further reported the existence of different local charge environments [79]. While it is tempting to associate these behaviors with nematic and magnetic domain breakup, and to speculate that the two charge environments could correspond to the two types of domain breakup, further analysis is needed to disentangle this from other possible effects. Indeed, because the spin $\frac{3}{2}$ of the ^{75}As nucleus experiences both dipolar and quadrupolar interactions [78], it would be valuable to quantitatively separate the nematic and magnetic fluctuation contributions to the spin-lattice relaxation rate. Moreover, a systematic analysis of the impact of annealing on the glassylike NMR response would be desirable. It is also interesting to note that ultrafast optical measurements in the magnetically ordered state of $BaFe_2As_2$ revealed the existence of two different relaxation time scales, a "slow" one (of the order of tens of picoseconds) and a "fast" one (of the order of picoseconds) [66]. While a different interpretation was proposed in that paper, additional experiments in samples subjected to different annealing regimens could help elucidate whether these two timescales are those that characterize the magnetic and nematic degrees of freedom in the RBFM.

We conclude by emphasizing that the RBFM should also describe realistic nematic phenomena in other quasi-2D quantum materials for which nematicity is a partially melted density-wave stripe state. Beyond the iron pnictides, nematicity in the cuprates has been proposed to arise from the partial melting of charge-stripe order [35]. In contrast to magnetic domains, but like nematic domains, charge-order domains can in principle also be probed via scanning tunneling microscopy (STM) [38,80]. This opens up the interesting prospect of a quantitative analysis to search for signatures of RBFM behavior in the STM data, similarly to what has been previously done using the RFIM [25].

ACKNOWLEDGMENTS

We thank A. Chakraborty, J. Freedberg, and E. D. Dahlberg for fruitful discussions. W.J.M. and R.M.F. were supported by the U. S. Department of Energy, Office of Science, Basic Energy Sciences, Materials Sciences and Engineering Division, under Award No. DE-SC0020045. T.V. was supported by the National Science Foundation under Grant No. DMR-1828489. T.V. and R.M.F. acknowledge the hospitality of KITP at UCSB, where the work was initiated. KITP is supported by the National Science Foundation under Grant No. NSF PHY-1748958. We thank the Minnesota Supercomputing Institute (MSI) at the University of Minnesota, where the numerical computations were performed.

APPENDIX A: GINZBURG-LANDAU EXPANSION OF THE RBFM

We first derive the coarse-grained effective field theory for the Ashkin-Teller model in the absence of any external strain. We then compare it to the known Ginzburg-Landau theory for the Ising J_1-J_2 model and discuss the mapping between the two models in the presence of an external strain.

For convenience, we write again the Ashkin-Teller Hamiltonian:

$$H = -\sum_{\langle ij\rangle}[J(\sigma_i\sigma_j+\tau_i\tau_j)+K\sigma_i\tau_i\sigma_j\tau_j]. \tag{A1}$$

Let $\tilde{J}_{ij}$ and $\tilde{K}_{ij}$ denote sparse $N\times N$ matrices whose nonzero elements J and K, respectively, connect nearest-neighbor sites. Then, the canonical partition function is given by

$$\mathcal{Z} = \mathrm{Tr}_{\{\sigma,\tau\}}\exp\left\{\frac{\beta}{2}\sum_{ij}[\tilde{J}_{ij}(\sigma_i\sigma_j+\tau_i\tau_j)+\tilde{K}_{ij}\sigma_i\tau_i\sigma_j\tau_j]\right\}, \tag{A2}$$

where β is the inverse temperature. From this expression, we identify three Hubbard-Stratonovich fields for the σ, τ, and $\sigma\tau$ degrees of freedom, which we denote as M_1, M_2, and φ. Making use of the corresponding Hubbard-Stratonovich transformations, the partition function becomes

$$\begin{aligned}\mathcal{Z} \propto \int & \mathfrak{D}M_1\mathfrak{D}M_2\mathfrak{D}\varphi \\ & \times\exp\Bigg\{-\frac{1}{2\beta}\sum_{ij}\Bigg(\sum_{\alpha=1,2}\tilde{J}^{-1}_{ij}M_{\alpha,i}M_{\alpha,j}+\tilde{K}^{-1}_{ij}\varphi_i\varphi_j\Bigg) \\ & +\sum_i V(M_{1,i},M_{2,i},\varphi_i)\Bigg\},\end{aligned} \tag{A3}$$

where the onsite potential function $V=V(x,y,z)$ is given by

$$\begin{aligned}V(x,y,z) &\equiv \log\{\mathrm{Tr}_{\sigma,\tau}\exp(x\sigma+y\tau+z\sigma\tau)\} \\ &= \log 4+\log[P_c(x,y,z)+P_s(x,y,z)],\end{aligned} \tag{A4}$$

with the functions $P_{c,s}$ being given by

$$P_c(x,y,z)=\cosh(x)\cosh(y)\cosh(z), \tag{A5}$$

$$P_s(x,y,z)=\sinh(x)\sinh(y)\sinh(z). \tag{A6}$$

The terms with coefficients $\tilde{J}^{-1}_{ij}$ and $\tilde{K}^{-1}_{ij}$ contribute to the "mass" for each field and also generate gradient terms allowed by symmetry. Neglecting these gradients for now, we write the partition function per site as

$$\begin{aligned}\mathcal{Z}_i \propto \int dM_{1,i}dM_{2,i}d\varphi_i\,\exp\Bigg\{&-\frac{1}{2\beta Jz}\Bigg(M_{1,i}^2+M_{2,i}^2+\frac{1}{g}\varphi_i^2\Bigg) \\ &+V(M_{1,i},M_{2,i},\varphi_i)\Bigg\},\end{aligned} \tag{A7}$$

where z is the number of nearest neighbors each site has and the dimensionless parameter $g\equiv K/J$. Hereafter, we omit the site index for simplicity.

For small fields and dropping the constant log 4, the potential is expanded as

$$\begin{aligned}V(M_1,M_2,\varphi) \approx{}& \frac{1}{2}\big(M_1^2+M_2^2+\varphi^2\big)+M_1M_2\varphi \\ &-\frac{1}{12}\big(M_1^4+M_2^4+\varphi^4\big).\end{aligned} \tag{A8}$$

Denoting the effective action with the expanded potential as S_{eff}, we can evaluate the φ integration in $\mathcal{Z}\propto\int dM_1dM_2d\varphi\,e^{-S_{\text{eff}}}$ upon noting that there is no φ-driven instability in the regime where the Ising J_1-J_2 model and the Ashkin-Teller model map onto one another, which corresponds to $g\in(0,1)$. In this case, we can neglect the φ^4 term, allowing us to integrate out the nematic field. We then obtain the effective magnetic free-energy density, defined by $\mathcal{Z}\propto\int dM_1dM_2\,e^{-\beta f_{\text{eff}}}$, as

$$\begin{aligned}\beta f_{\text{eff}} ={}& \frac{1}{2}\Bigg(\frac{1}{\beta Jz}-1\Bigg)\big(M_1^2+M_2^2\big)+\frac{1}{12}\big(M_1^4+M_2^4\big) \\ &-\frac{\beta Jgz}{2(1-\beta Jgz)}(M_1M_2)^2.\end{aligned} \tag{A9}$$

We can now add back the lowest-order gradient terms allowed by symmetry. Then, after defining $r\equiv 1/\beta Jz-1$, we obtain the Ginzburg-Landau free-energy density of the Ashkin-Teller model as

$$\begin{aligned}\beta f_{\text{eff}} ={}& \frac{1}{2}\sum_{\alpha=1}^{2}\Bigg[rM_\alpha^2+\frac{1}{6}M_\alpha^4+c^2(\nabla M_\alpha)^2\Bigg] \\ &-\frac{\beta Jgz}{2(1-\beta Jgz)}(M_1M_2)^2,\end{aligned} \tag{A10}$$

where c, called the stiffness coefficient, is a function of the microscopic Ising exchange J. We note that the free energy above retains a fourfold symmetry due to the symmetry between the σ and τ Ising degrees of freedom.

This free-energy expansion can be compared to that of the Ising J_1-J_2 model. Using the results from Refs. [36,37], the Ginzburg-Landau expansion for the free energy of the J_1-J_2

model is given by

$$\beta f_{\text{eff}} = \frac{1}{2}\sum_{\alpha=1}^{2}\left[\tilde{r}\phi_\alpha^2 + u\phi_\alpha^4 + \tilde{c}^2(\nabla\phi_\alpha)^2\right] - \alpha(\phi_1\phi_2)^2. \quad \text{(A11)}$$

Here, $\phi_{1,2}$ are the two scalar staggered sublattice magnetizations, and the nematic variable is given by their product $\phi_1\phi_2$. Moreover, $\tilde{r}$ is the distance from the critical point, $u > 0$, and $\tilde{c}$ is the stiffness coefficient. The coefficient of the last term, $\alpha > 0$, is generated from either quantum or thermal fluctuations, and stabilizes the nematic phase through the order-by-disorder mechanism [36,37,81].

Comparing the two low-energy effective theories in Eqs. (A10) and (A11), we conclude that they indeed share the same low-energy behavior.

Consider now the presence of external strain ε, which favors a nematic order parameter $\varphi \sim M_1M_2$ with same sign as that of ε. To leading order, it introduces a new quadratic term in the free-energy expansion of the Ashkin-Teller model in Eq. (A10):

$$\delta(\beta f_{\text{eff}}) = -\beta\varepsilon M_1M_2. \quad \text{(A12)}$$

Analogously, the same quadratic coupling, but for the nematic order parameter $\phi_1\phi_2$, emerges in the free-energy expansion of the Ising J_1-J_2 model. As a result, the mapping between the two models should hold also in the presence of random strain.

APPENDIX B: NUMERICAL METHODS

1. Adaptive simulated annealing

We used simulated annealing to get a qualitative picture of the emergence of two length scales in the RBFM induced by the random Baxter field. To do so, we had to simulate the system at low temperatures to disentangle the disorder effects from thermal fluctuation effects. At low temperatures, the effects of disorder are more pronounced, but this leads to the possibility of a simulation getting stuck in a metastable state if one were to simply set the temperature to be low. Simulated annealing provides a physically motivated way to move a simulation into lower-energy states by thermally activated tunneling through energy barriers separating local energy minima [82]. It does so by first raising the temperature of the simulation above all energy barriers, and then slowly lowering the temperature of the system, or "annealing" it, until the lowest temperature is reached. Our algorithm is "adaptive" in the sense that it continues simulating at a single temperature if it notices the system is not yet equilibrated.

A conventional simulated annealing regimen is performed according to the following steps. First, one initializes the system in some state. Then, an initial temperature is chosen and the system is equilibrated using some updating scheme satisfying detailed balance. From there, the system is annealed by lowering the temperature slowly enough such that it equilibrates at each new temperature until it reaches some defined lowest temperature [82].

Our adaptive approach works by defining equilibrium based on time records of the energy that are L_t sweeps long. The time records are split into two blocks and the system is said to be equilibrated if one of the following two conditions are met:

(1) The energy does not vary in both blocks of Monte Carlo time,

(2) The average energy of the second block is within one standard deviation of the first *and* the variance of the energy in the second block is within a specified tolerance η of that in the first block.

The first condition is that the system is frozen in a particular energy state: this may only occur at low temperatures. Condition 2 is that measurements of the energy and specific heat [through Eq. (12)] are statistically time independent. If neither of these two conditions are met, then the system continues its Markov chain at the same temperature and computes another time record of the energy.

The numerical parameters used in our simulated annealing run are as follows. We initialized the magnetic degrees of freedom in the RBFM with equal probability of being ±1 at each site, which corresponds to a microstate with maximal entropy. We used the initial temperature of $T_i \equiv 2.269\,J$ corresponding to the 2D Ising critical temperature. We equilibrated the system using a single-site Metropolis updating scheme over two time record blocks, each of size $2^{10} = 1024$ sweeps, making $L_t = 2048$ sweeps long. The specific-heat tolerance was set to $\eta = 0.05$. We chose a cooling regimen corresponding to

$$T_j = T_i\left(\frac{T_f}{T_i}\right)^{j/N_{\text{steps}}}, \quad \text{(B1)}$$

where T_j is the temperature of the jth simulated annealing step, with $j \in \{1, 2, \ldots, N_{\text{steps}}\}$, and T_f is the final temperature. The data shown in Figs. 4 and 5 from simulated annealing had a minimum temperature of $T_f = 0.269\,J$ and ran over $N_{\text{steps}} = 150$ steps. Thus, the temperature of the simulation decreased by about 1.4% between steps. At this small percentage, we noticed that each step would typically require less than five adaptive iterations to equilibrate.

2. Wang-Landau sampling

We employ the replica-exchange Wang-Landau (WL) Monte Carlo technique recently developed for complex energy landscapes [60–62] to simulate Eq. (8). This technique expands on the WL sampling algorithm known for its ability to quickly calculate thermodynamic properties at arbitrary temperatures after obtaining a system's microcanonical density of states [58,59].

In the WL algorithm, the density of states g at a given energy E is obtained iteratively by performing a random walk through energy space. It is calculated by keeping track of two histograms during a random walk through the system's phase space. The first is the approximation of $g(E)$ and the other one is typically called the "energy histogram," denoted by $\mathcal{H}(E)$. The energy histogram is used to ensure the sampling of the phase space is uniform throughout the simulation.

The density of states is initially approximated as a constant of value one whereas the energy histogram is set to be a constant zero. During the random walk, transitions from energy E to E' are accepted with probability

$$\mathcal{W}(E \to E') = \min\left\{1, \frac{g(E)}{g(E')}\right\}. \quad \text{(B2)}$$

In our simulations, new energy states are generated as single-spin updates of one Ising spin color for a single lattice sweep while the other one is quenched. Regardless of whether the transition is accepted, one updates both g and $\mathcal{H}$ at the resulting energy. The increment for the energy histogram always comes from the addition of 1 in the resulting energy bin. The density of states in that energy bin, meanwhile, is scaled by a factor f_i in the ith iteration, where f_i is given by

$$f_i = f_1^{\frac{1}{2^{i-1}}}. \tag{B3}$$

A typical value for the initial increment is $f_1 = e$. Each iteration ends once the energy histogram is "flat." In our simulations, "flatness" was measured according to a tolerance $\epsilon \leqslant 0.3$ such that

$$\frac{\max\{\mathcal{H}(E)\} - \min\{\mathcal{H}(E)\}}{\min\{\mathcal{H}(E)\}} < \epsilon. \tag{B4}$$

After an iteration, the energy histogram is reset to zero and, conventionally, the density of states is left untouched. However, since $g(E)$ updated in the WL scheme is only the relative density of states, after each iteration we scale the density of states by its minimum value to maintain numerical sensitivity to the decreasing f_i.

The microcanonical density of states is considered "converged" when its increment is smaller than a predefined value. In our case, this value was $f_i \leqslant 1 + 5 \times 10^{-7}$ in the most demanding cases ($K = 0$ simulations), although we typically used a more stringent condition of $f_i \leqslant 1 + 1 \times 10^{-7}$ when possible ($K > 0$ simulations). Upon convergence, the thermodynamic observables obtained by energetic moments can be computed from the density of states at any temperature T since the partition function is given by

$$\mathcal{Z} = \sum_E g(E)\, e^{-E/T}. \tag{B5}$$

For example, $\langle E^n \rangle$ for some power n is obtained by

$$\langle E^n \rangle = \frac{1}{\mathcal{Z}} \sum_E g(E)\, e^{-E/T}\, E^n, \tag{B6}$$

from which the specific heat, measured as the heat capacity per lattice site, is calculated from Eq. (12).

One can extend the WL algorithm to a joint density of states if nonenergy moments of the Boltzmann distribution are required [58,59]. This would require a joint energy histogram whose flatness would then be measured in the higher-dimensional space. However, to speed our simulations, we instead kept track of another histogram for each nonenergy observable of interest; $|\sigma|$ and $|\tau|$ are a couple, for example. These observable histograms do not influence the convergence rate of the simulation as they do not appear in our flatness metric. Instead, they capture the mean value of nonenergy observables within each energy bin. These means were updated as a cumulative moving average per energy bin for each WL update. Denoting such an observable as A, and its histogram of mean values in energy space as $\overline{A}(E)$, then its expectation value at any temperature is

$$\langle A \rangle = \frac{1}{\mathcal{Z}} \sum_E g(E)\, e^{-E/T}\, \overline{A}(E). \tag{B7}$$

In our typical simulation, there are more than 10^7 individual measurements taken for each observable in each energy bin. These measurements per bin likely suffer from autocorrelations, but we obtain error bars on thermodynamic observables by running simulations in parallel with different seeds for the random number generators and then averaging the results.

3. Replica-exchange Wang-Landau sampling

WL sampling is a fast Monte Carlo method for studying small and simple systems. When applied to larger systems, or systems with complex energy landscapes, the time to solution increases rapidly. Thus, to study the effect of the random strain disorder in Eq. (8), we employ a replica-exchange WL sampling algorithm which is a massively parallel extension of the WL procedure above [60–62].

Its ability to speed up WL sampling comes in three parts. First, it divides the phase-space volume into a set of N_w equally sized, overlapping energy windows within which $g(E)$ is approximated using the WL scheme. Second, the energy windows in the overlapping regions are occasionally allowed to exchange states with a probability:

$$\mathcal{W}(\{E_1, E_2\} \to \{E_2, E_1\}) = \min\left\{1, \frac{g_1(E_1)}{g_1(E_2)} \cdot \frac{g_2(E_2)}{g_2(E_1)}\right\}, \tag{B8}$$

where E_1 and E_2 are the energies of the two windows undergoing exchange and g_1 and g_2 are their density of states. From Eq. (B2), one sees that when the exchange is not guaranteed, Eq. (B8) is simply the product of the WL transition probabilities for the first energy window to move from E_1 to E_2 and for the second one to move from E_2 to E_1.

When an exchange update is accepted, then the two energy windows involved swap their spin configurations. The density of states and energy histogram in each window are always incremented after an exchange attempt, regardless of whether the exchange actually occurred. In our simulations, an exchange attempt was made between two adjacent energy windows after each sweep of the lattice to increase the number of exchanges. This facilitates information dispersal through the divided phase space.

The third part of replica-exchange WL sampling comes by adding n-independent WL random walkers, or *replicas*, to each of the N_w energy windows. By increasing n, the number of exchanges increases. The optimal speedup of replica-exchange WL over standard WL comes from a combination of the size of the overlap, the number of energy windows, the number of replicas per window, and how often the exchange updates are attempted. The optimizing combination of these parameters is model dependent, but we found success when allowing a 75%–80% overlap between energy windows with only 2 ($K > 0$) or 1 ($K = 0$) replicas per window. When $K > 0$, the number of windows was set to be $N_w = 2L$. However, when $K = 0$ with a nonzero disorder strength, we found that a smaller number of windows allowed for the fastest convergence with $N_w = 24$.

In the replica-exchange WL scheme, the simulation is finished when each density of states in each energy window is converged. If some windows converge before others, then they continue to perform replica-exchange WL updates until

TABLE I. Number of replica-exchange WL simulation disorder configurations for each set of model parameters for a system size $L = 40$. The columns with K defined correspond to the RBFM while the RFIM column is for the random-field Ising model. These parameters were used in all figures other than Fig. 7.

Disorder strength	$K = 0.5\,J$	$K = 0$	RFIM
$\varepsilon = 0.0\,J$	64	64	128
$\varepsilon = 0.2\,J$	96	96	128
$\varepsilon = 0.5\,J$	94	120	126
$\varepsilon = 0.8\,J$	246	147	148

TABLE II. Number of replica-exchange WL simulation disorder configurations for each model parameter for the systems in Fig. 7.

System size	$\varepsilon = 0.0\,J$	$\varepsilon = 0.5\,J$
$L = 24$	64	128
$L = 32$	64	124
$L = 40$	64	114
$L = 48$	64	173
$L = 56$	64	78

the rest of the windows converge as well. This allows information from the faster-converging regions of phase space to still diffuse to the slower regions. When there are multiple replicas in a single energy window, the window itself moves from one iteration to the next only when every replica's energy histogram is flat. When this happens, the density of states from each replica is scaled as for normal WL sampling, and then the densities of states from all the replicas are averaged and redistributed before the next iteration is performed. The observables from all the walkers within a single energy window, however, are only averaged after the simulation is complete.

Once complete, the density of states over the full phase space is assembled by stitching together the individual density of states from each energy window. This procedure is carried out within the overlapping regions by finding the energy bin where the microcanonical temperatures $T^{-1} = d\,\log g(E)/dE$ are the closest between a lower-energy window and a higher-energy window. The differentiation is performed with a finite-difference formula accurate up to fourth order in the bin size. The observables are averaged within the overlapping regions. Since multiple windows may be overlapping in the same region, this may lead to an overwriting of the final density of states. We do not stop this from happening; however, the observables are still averaged across all overlapping windows such that statistics from any energy window with an overwritten density of states is not lost.

4. Disorder averaging

The Hamiltonian in Eq. (8) was simulated for a single-field configuration, or single quenched set of random Baxter-field variables $\{\varepsilon_i\}$, using the replica-exchange WL procedure. Then, the thermodynamics from many field configurations were averaged to obtain our final results.

Denoting the thermodynamic average of an observable A in disorder configuration j by $\langle A\rangle_j$, the disorder-averaged expectation value over M-field configurations was calculated as

$$[\![\langle A\rangle]\!] = \frac{1}{M}\sum_{j=1}^{M}\langle A\rangle_j, \tag{B9}$$

where the double brackets $[\![\cdot]\!]$ represent the disorder average. Its standard error of the mean was computed as

$$\delta A_{\mathrm{d.a.}} = \left[\frac{1}{M(M-1)}\sum_{j=1}^{M}(\langle A\rangle_j - [\![\langle A\rangle]\!])^2\right]^{1/2}. \tag{B10}$$

Tables I and II show the number of distinct disorder configuration averaged over for the replica-exchange WL simulations. The differences in the numbers of disorder configurations are due to the increasing difficulty to converge the simulations for large disorder strengths.

5. Replica-exchange Wang-Landau simulation code details

The replica-exchange WL parallelization was performed processorwise on supercomputing nodes at the Minnesota Supercomputing Institute. The replica-exchange WL code was benchmarked against the 2D clean Ising model and 2D clean ATM, as well as a 2D RFIM, all on a periodic square lattice. The only difference in the code between these test models and our ATM is the Hamiltonian selected at compile time. Any numerical analysis performed after the simulations were complete, such as disorder averaging, plotting, etc., was scripted using Python 3 making use of the SCIPY libraries. The source code and job scripts can be found at Ref. [83].

[1] T. Vojta, Phases and phase transitions in disordered quantum systems, in *AIP Conference Proceedings Volume 1550* (AIP, Melville, NY, 2013), p. 188.

[2] T. Vojta, Disorder in quantum many-body systems, Annu. Rev. Condens. Matter Phys. **10**, 233 (2019).

[3] R. Balian and N. R. Werthamer, Superconductivity with pairs in a relative p wave, Phys. Rev. **131**, 1553 (1963).

[4] Y. Dalichaouch, M. C. de Andrade, D. A. Gajewski, R. Chau, P. Visani, and M. B. Maple, Impurity Scattering and Triplet Superconductivity in UPt$_3$, Phys. Rev. Lett. **75**, 3938 (1995).

[5] A. P. Mackenzie, R. K. W. Haselwimmer, A. W. Tyler, G. G. Lonzarich, Y. Mori, S. Nishizaki, and Y. Maeno, Extremely Strong Dependence of Superconductivity on Disorder in Sr$_2$RuO$_4$, Phys. Rev. Lett. **80**, 161 (1998).

[6] A. I. Larkin, Effect of inhomogeneities on the structure of the mixed state of superconductors, Zh. Eksp. Theor. Fiz. **58**, 1466 (1970) [Sov. Phys.–JETP **31**, 784 (1970)].

[7] G. Grüner, The dynamics of charge-density waves, Rev. Mod. Phys. **60**, 1129 (1988).

[8] T. Giamarchi and P. Le Doussal, Elastic Theory of Pinned Flux Lattices, Phys. Rev. Lett. **72**, 1530 (1994).

[9] S. A. Kivelson, E. Fradkin, and V. J. Emery, Electronic liquid-crystal phases of a doped Mott insulator, Nature (London) **393**, 550 (1998).

[10] R. M. Fernandes, A. V. Chubukov, and J. Schmalian, What drives nematic order in iron-based superconductors? Nat. Phys. **10**, 97 (2014).

[11] E. Fradkin, S. A. Kivelson, M. J. Lawler, J. P. Eisenstein, and A. P. Mackenzie, Nematic Fermi fluids in condensed matter physics, Annu. Rev. Condens. Matter Phys. **1**, 153 (2010).

[12] Y. Qi and C. Xu, Global phase diagram for magnetism and lattice distortion of iron-pnictide materials, Phys. Rev. B **80**, 094402 (2009).

[13] R. M. Fernandes, L. H. VanBebber, S. Bhattacharya, P. Chandra, V. Keppens, D. Mandrus, M. A. McGuire, B. C. Sales, A. S. Sefat, and J. Schmalian, Effects of Nematic Fluctuations on the Elastic Properties of Iron Arsenide Superconductors, Phys. Rev. Lett. **105**, 157003 (2010).

[14] A. Cano, M. Civelli, I. Eremin, and I. Paul, Interplay of magnetic and structural transitions in iron-based pnictide superconductors, Phys. Rev. B **82**, 020408(R) (2010).

[15] J.-H. Chu, H.-H. Kuo, J. G. Analytis, and I. R. Fisher, Divergent nematic susceptibility in an iron arsenide superconductor, Science **337**, 710 (2012).

[16] A. E. Böhmer, P. Burger, F. Hardy, T. Wolf, P. Schweiss, R. Fromknecht, M. Reinecker, W. Schranz, and C. Meingast, Nematic Susceptibility of Hole-Doped and Electron-Doped $BaFe_2As_2$ Iron-Based Superconductors from Shear Modulus Measurements, Phys. Rev. Lett. **112**, 047001 (2014).

[17] E. W. Carlson, K. A. Dahmen, E. Fradkin, and S. A. Kivelson, Hysteresis and Noise from Electronic Nematicity in High-Temperature Superconductors, Phys. Rev. Lett. **96**, 097003 (2006).

[18] Y. L. Loh, E. W. Carlson, and K. A. Dahmen, Noise predictions for STM in systems with local electron nematic order, Phys. Rev. B **81**, 224207 (2010).

[19] E. Carlson and K. Dahmen, Using disorder to detect locally ordered electron nematics via hysteresis, Nat. Commun. **2**, 379 (2011).

[20] E. Carlson, S. Liu, B. Phillabaum, and K. A. Dahmen, Decoding spatial complexity in strongly correlated electronic systems, J. Supercond. Novel Magn. **28**, 1237 (2015).

[21] Y. Imry and S.-K. Ma, Random-Field Instability of the Ordered State of Continuous Symmetry, Phys. Rev. Lett. **35**, 1399 (1975).

[22] K. Binder, Random-field induced interface widths in Ising systems, Z. Phys. B **50**, 343 (1983).

[23] T. Nattermann, Theory of the random field Ising model, in *Spin Glasses and Random Fields* (World Scientific, Singapore, 1998), pp. 277–298.

[24] O. Zachar and I. Zaliznyak, Dimensional Crossover and Charge Order in Half-Doped Manganites and Cobaltites, Phys. Rev. Lett. **91**, 036401 (2003).

[25] B. Phillabaum, E. Carlson, and K. Dahmen, Spatial complexity due to bulk electronic nematicity in a superconducting underdoped cuprate, Nat. Commun. **3**, 915 (2012).

[26] P. Wiecki, R. Zhou, M.-H. Julien, A. E. Böhmer, and J. Schmalian, Edwards-Anderson parameter and local Ising nematicity in FeSe revealed via NMR spectral broadening, Phys. Rev. B **104**, 125134 (2021).

[27] H.-H. Kuo, J.-H. Chu, J. C. Palmstrom, S. A. Kivelson, and I. R. Fisher, Ubiquitous signatures of nematic quantum criticality in optimally doped Fe-based superconductors, Science **352**, 958 (2016).

[28] E. Fradkin, S. A. Kivelson, and J. M. Tranquada, Colloquium: Theory of intertwined orders in high temperature superconductors, Rev. Mod. Phys. **87**, 457 (2015).

[29] R. M. Fernandes, P. P. Orth, and J. Schmalian, Intertwined Vestigial Order in Quantum Materials: Nematicity and Beyond, Annu. Rev. Condens. Matter Phys. **10**, 133 (2019).

[30] O. Cyr-Choinière, G. Grissonnanche, S. Badoux, J. Day, D. A. Bonn, W. N. Hardy, R. Liang, N. Doiron-Leyraud, and L. Taillefer, Two types of nematicity in the phase diagram of the cuprate superconductor $YBa_2Cu_3O_y$, Phys. Rev. B **92**, 224502 (2015).

[31] A. J. Achkar, M. Zwiebler, C. McMahon, F. He, R. Sutarto, I. Djianto, Z. Hao, M. J. P. Gingras, M. Hücker, G. D. Gu, A. Revcolevschi, H. Zhang, Y.-J. Kim, J. Geck, and D. G. Hawthorn, Nematicity in stripe-ordered cuprates probed via resonant x-ray scattering, Science **351**, 576 (2016).

[32] C. Eckberg, D. J. Campbell, T. Metz, J. Collini, H. Hodovanets, T. Drye, P. Zavalij, M. H. Christensen, R. M. Fernandes, S. Lee *et al.*, Sixfold enhancement of superconductivity in a tunable electronic nematic system, Nat. Phys. **16**, 346 (2020).

[33] S. Seo, X. Wang, S. M. Thomas, M. C. Rahn, D. Carmo, F. Ronning, E. D. Bauer, R. D. dos Reis, M. Janoschek, J. D. Thompson, R. M. Fernandes, and P. F. S. Rosa, Nematic State in $CeAuSb_2$, Phys. Rev. X **10**, 011035 (2020).

[34] D. C. Johnston, The puzzle of high temperature superconductivity in layered iron pnictides and chalcogenides, Adv. Phys. **59**, 803 (2010).

[35] L. Nie, G. Tarjus, and S. A. Kivelson, Quenched disorder and vestigial nematicity in the pseudogap regime of the cuprates, Proc. Natl. Acad. Sci. USA **111**, 7980 (2014).

[36] C. Xu, M. Müller, and S. Sachdev, Ising and spin orders in the iron-based superconductors, Phys. Rev. B **78**, 020501(R) (2008).

[37] C. Fang, H. Yao, W.-F. Tsai, J. P. Hu, and S. A. Kivelson, Theory of electron nematic order in LaFeAsO, Phys. Rev. B **77**, 224509 (2008).

[38] A. Mesaros, K. Fujita, H. Eisaki, S. Uchida, J. C. Davis, S. Sachdev, J. Zaanen, M. J. Lawler, and E.-A. Kim, Topological defects coupling smectic modulations to intra-unit-cell nematicity in cuprates, Science **333**, 426 (2011).

[39] Y. Kamiya, N. Kawashima, and C. D. Batista, Dimensional crossover in the quasi-two-dimensional Ising-O(3) model, Phys. Rev. B **84**, 214429 (2011).

[40] R. M. Fernandes, A. V. Chubukov, J. Knolle, I. Eremin, and J. Schmalian, Preemptive nematic order, pseudogap, and orbital order in the iron pnictides, Phys. Rev. B **85**, 024534 (2012).

[41] Y. Wang and A. Chubukov, Charge-density-wave order with momentum $(2q, 0)$ and $(0, 2q)$ within the spin-fermion model: Continuous and discrete symmetry breaking, preemptive composite order, and relation to pseudogap in hole-doped cuprates, Phys. Rev. B **90**, 035149 (2014).

[42] L. Nie, A. V. Maharaj, E. Fradkin, and S. A. Kivelson, Vestigial nematicity from spin and/or charge order in the cuprates, Phys. Rev. B **96**, 085142 (2017).

[43] P. P. Orth, B. Jeevanesan, R. M. Fernandes, and J. Schmalian, Enhanced nematic fluctuations near an antiferromagnetic Mott insulator and possible application to high-T_c cuprates, npj Quantum Mater. **4**, 4 (2019).

[44] S. Mukhopadhyay, R. Sharma, C. K. Kim, S. D. Edkins, M. H. Hamidian, H. Eisaki, S.-I. Uchida, E.-A. Kim, M. J. Lawler, A. P. Mackenzie, J. C. S. Davis, and K. Fujita, Evidence for a vestigial nematic state in the cuprate pseudogap phase, Proc. Natl. Acad. Sci. USA **116**, 13249 (2019).

[45] R. M. Fernandes, A. E. Böhmer, C. Meingast, and J. Schmalian, Scaling Between Magnetic and Lattice Fluctuations in Iron Pnictide Superconductors, Phys. Rev. Lett. **111**, 137001 (2013).

[46] P. Chandra, P. Coleman, and A. I. Larkin, Ising Transition in Frustrated Heisenberg Models, Phys. Rev. Lett. **64**, 88 (1990).

[47] S. Jin, A. Sen, and A. W. Sandvik, Ashkin-Teller Criticality and Pseudo-First-Order Behavior in a Frustrated Ising Model on the Square Lattice, Phys. Rev. Lett. **108**, 045702 (2012).

[48] S. Jin, A. Sen, W. Guo, and A. W. Sandvik, Phase transitions in the frustrated Ising model on the square lattice, Phys. Rev. B **87**, 144406 (2013).

[49] Q. Si and E. Abrahams, Strong Correlations and Magnetic Frustration in the High T_c Iron Pnictides, Phys. Rev. Lett. **101**, 076401 (2008).

[50] P. Dai, Antiferromagnetic order and spin dynamics in iron-based superconductors, Rev. Mod. Phys. **87**, 855 (2015).

[51] M. H. Christensen, J. Kang, B. M. Andersen, I. Eremin, and R. M. Fernandes, Spin reorientation driven by the interplay between spin-orbit coupling and Hund's rule coupling in iron pnictides, Phys. Rev. B **92**, 214509 (2015).

[52] M. Suzuki, New universality of critical exponents, Prog. Theor. Phys. **51**, 1992 (1974).

[53] R. V. Ditzian, J. R. Banavar, G. S. Grest, and L. P. Kadanoff, Phase diagram for the Ashkin-Teller model in three dimensions, Phys. Rev. B **22**, 2542 (1980).

[54] T. Vojta, Rare region effects at classical, quantum and nonequilibrium phase transitions, J. Phys. A: Math. Gen. **39**, R143 (2006).

[55] S. S. Kunwar, A. Sen, T. Vojta, and R. Narayanan, Tuning a random-field mechanism in a frustrated magnet, Phys. Rev. B **98**, 024206 (2018).

[56] X. Ye, R. Narayanan, and T. Vojta, Stripe order, impurities, and symmetry breaking in a diluted frustrated magnet, Phys. Rev. B **105**, 024201 (2022).

[57] M. Aizenman and J. Wehr, Rounding of First-Order Phase Transitions in Systems with Quenched Disorder, Phys. Rev. Lett. **62**, 2503 (1989).

[58] F. Wang and D. P. Landau, Efficient, Multiple-Range Random Walk Algorithm to Calculate the Density of States, Phys. Rev. Lett. **86**, 2050 (2001).

[59] F. Wang and D. P. Landau, Determining the density of states for classical statistical models: A random walk algorithm to produce a flat histogram, Phys. Rev. E **64**, 056101 (2001).

[60] T. Vogel, Y. W. Li, T. Wüst, and D. P. Landau, Generic, Hierarchical Framework for Massively Parallel Wang-Landau Sampling, Phys. Rev. Lett. **110**, 210603 (2013).

[61] T. Vogel, Y. W. Li, T. Wüst, and D. P. Landau, Scalable replica-exchange framework for Wang-Landau sampling, Phys. Rev. E **90**, 023302 (2014).

[62] T. Vogel, Y. W. Li, and D. P. Landau, A practical guide to replica-exchange Wang-Landau simulations, J. Phys.: Conf. Ser. **1012**, 012003 (2018).

[63] N. Metropolis, A. W. Rosenbluth, M. N. Rosenbluth, A. H. Teller, and E. Teller, Equation of state calculations by fast computing machines, J. Chem. Phys. **21**, 1087 (1953).

[64] P. C. Hohenberg and B. I. Halperin, Theory of dynamic critical phenomena, Rev. Mod. Phys. **49**, 435 (1977).

[65] P. M. Chaikin and T. C. Lubensky, *Principles of Condensed Matter Physics* (Cambridge University Press, Cambridge, 1995).

[66] A. Patz, T. Li, S. Ran, R. M. Fernandes, J. Schmalian, S. L. Bud'ko, P. C. Canfield, I. E. Perakis, and J. Wang, Ultrafast observation of critical nematic fluctuations and giant magnetoelastic coupling in iron pnictides, Nat. Commun. **5**, 3229 (2014).

[67] D. K. C. MacDonald, *Noise and Fluctuations: An Introduction (Dover Books on Physics)* (Dover, New York, 2006), Chap. 2, pp. 44–53.

[68] P. Dutta and P. M. Horn, Low-frequency fluctuations in solids: $\frac{1}{f}$ noise, Rev. Mod. Phys. **53**, 497 (1981).

[69] M. B. Weissman, $\frac{1}{f}$ noise and other slow, nonexponential kinetics in condensed matter, Rev. Mod. Phys. **60**, 537 (1988).

[70] S. F. Edwards and P. W. Anderson, Theory of spin glasses, J. Phys. F: Met. Phys. **5**, 965 (1975).

[71] K. Binder and A. P. Young, Spin glasses: Experimental facts, theoretical concepts, and open questions, Rev. Mod. Phys. **58**, 801 (1986).

[72] J. L. Niedziela, M. A. McGuire, and T. Egami, Local structural variation as source of magnetic moment reduction in $BaFe_2As_2$, Phys. Rev. B **86**, 174113 (2012).

[73] S. Ran, S. L. Bud'ko, D. K. Pratt, A. Kreyssig, M. G. Kim, M. J. Kramer, D. H. Ryan, W. N. Rowan-Weetaluktuk, Y. Furukawa, B. Roy, A. I. Goldman, and P. C. Canfield, Stabilization of an ambient-pressure collapsed tetragonal phase in $CaFe_2As_2$ and tuning of the orthorhombic-antiferromagnetic transition temperature by over 70 k via control of nanoscale precipitates, Phys. Rev. B **83**, 144517 (2011).

[74] T. R. Forrest, P. N. Valdivia, C. R. Rotundu, E. Bourret-Courchesne, and R. J. Birgeneau, The effects of post-growth annealing on the structural and magnetic properties of $BaFe_2As_2$, J. Phys.: Condens. Matter **28**, 115702 (2016).

[75] A. Jesche, C. Krellner, M. de Souza, M. Lang, and C. Geibel, Coupling between the structural and magnetic transition in CeFeAsO, Phys. Rev. B **81**, 134525 (2010).

[76] F. Hammerath, U. Gräfe, T. Kühne, H. Kühne, P. L. Kuhns, A. P. Reyes, G. Lang, S. Wurmehl, B. Büchner, P. Carretta, and H.-J. Grafe, Progressive slowing down of spin fluctuations in underdoped $LaFeAsO_{1-x}F_x$, Phys. Rev. B **88**, 104503 (2013).

[77] A. P. Dioguardi, M. M. Lawson, B. T. Bush, J. Crocker, K. R. Shirer, D. M. Nisson, T. Kissikov, S. Ran, S. L. Bud'ko, P. C. Canfield, S. Yuan, P. L. Kuhns, A. P. Reyes, H.-J. Grafe, and N. J. Curro, NMR evidence for inhomogeneous glassy behavior driven by nematic fluctuations in iron arsenide superconductors, Phys. Rev. B **92**, 165116 (2015).

[78] A. P. Dioguardi, T. Kissikov, C. H. Lin, K. R. Shirer, M. M. Lawson, H.-J. Grafe, J.-H. Chu, I. R. Fisher, R. M. Fernandes, and N. J. Curro, NMR Evidence for Inhomogeneous Nematic Fluctuations in $\mathrm{BaFe_2(As_{1-x}P_x)_2}$, Phys. Rev. Lett. **116**, 107202 (2016).

[79] G. Lang, H.-J. Grafe, D. Paar, F. Hammerath, K. Manthey, G. Behr, J. Werner, and B. Büchner, Nanoscale Electronic Order in Iron Pnictides, Phys. Rev. Lett. **104**, 097001 (2010).

[80] M. Lawler, K. Fujita, J. Lee, A. Schmidt, Y. Kohsaka, C. K. Kim, H. Eisaki, S. Uchida, J. Davis, J. Sethna *et al.*, Intra-unit-cell electronic nematicity of the high-T_c copper-oxide pseudogap states, Nature (London) **466**, 347 (2010).

[81] C. L. Henley, Ordering Due to Disorder in a Frustrated Vector Antiferromagnet, Phys. Rev. Lett. **62**, 2056 (1989).

[82] W. H. Press, S. A. Teukolsky, W. T. Vetterling, and B. P. Flannery, *Numerical Recipes: The Art of Scientific Computing* (Cambridge University Press, Cambridge, 2007), Chap. 10, pp. 549–555.

[83] W. J. Meese, REWL Simulator, GitHub Repository, https://github.com/meese-wj/REWL_Simulator.